The Journal of Chemical Physics

AIP Publishing

Phase behavior of metastable water from large-scale simulations of a quantitatively accurate model near ambient conditions: The liquid-liquid critical point.

Luis Enrique Coronas[1, 2, a)] and Giancarlo Franzese[1, 2]
[1)]*Secció de Física Estadística i Interdisciplinària, Departament de Física de la Matèria Condensada, Facutat de Física, University of Barcelona, Martí i Franquès 1, Barcelona 08028, Spain*
[2)]*Institute of Nanoscience and Nanotechnology (IN2UB), University of Barcelona, Martí i Franquès 1, Barcelona 08028, Spain*[b)]

(*Electronic mail: gfranzese@ub.edu)

(Dated: 7 August 2024)

The molecular mechanisms of water's unique anomalies are still debated. Experimental challenges have led to simulations suggesting a liquid-liquid (LL) phase transition, culminating in the supercooled region's LL critical point (LLCP). Computational expense, small system sizes, and the reliability of water models often limit these simulations. We adopt the CVF model, which is reliable, transferable, scalable, and efficient across a wide range of temperatures and pressures around ambient conditions. By leveraging the timescale separation between fast hydrogen bonds and slow molecular coordinates, the model allows a thorough exploration of the metastable phase diagram of liquid water. Using advanced numerical techniques to bypass dynamical slowing down, we perform finite-size scaling on larger systems than those used in previous analyses. Our study extrapolates thermodynamic behavior in the infinite-system limit, demonstrating the existence of the LLCP in the 3D Ising universality class in the low-temperature, low-pressure side of the line of temperatures of maximum density, specifically at $T_C = 186 \pm 4$ K and $P_C = 174 \pm 14$ MPa, at the end of a liquid-liquid phase separation stretching up to approximately 200 MPa. These predictions align with recent experimental data and sophisticated models, highlighting that hydrogen bond cooperativity governs the LLCP and the origin of water anomalies. We also observe substantial cooperative fluctuations in the hydrogen bond network at scales larger than 10 nm, even at temperatures relevant to biopreservation. These findings have significant implications for nanotechnology and biophysics, providing new insights into water's behavior under varied conditions.

I. INTRODUCTION

Water is essential in our lives, but its complex nature still raises many unresolved questions[1–4]. It is unique compared to other liquids for its more than 60 anomalies[5], such as a density maximum at around 4°C, or the large increase of its response functions upon cooling, when instead a decrease would be expected for usual liquids[1,4,6].

Several scenarios have been suggested to explain these properties[4,7–10]. The theory[11] has shown that all these scenarios stem from a general thermodynamic description and differ in the ratio between the intensity of the cooperative component[12] and the covalent component[13] of the hydrogen bond (HB) network. The estimate of this ratio supports[11] that water follows the scenario originally proposed by Poole et al.[8] based on molecular dynamic simulations. Poole and coworkers conceived that water undergoes a liquid-liquid phase transition (LLPT) between low-density liquid (LDL) and high-density liquid (HDL) phases, ending in a liquid-liquid critical point (LLCP) in the supercooled region. Several water models, ranging from atomistic to machine-learned *ab initio* quality force fields[14], have supported this hypothesis over the years, generating a large amount of numerical data that have dissipated criticisms and doubts about the theoretical possibility of such a scenario[15]. Yet, no experiment has shown the existence of a liquid-liquid phase transition in deeply supercooled water due to the difficulty in avoiding crystallization[16].

To date, substantial evidence supports the LLCP hypothesis based on multiple experiments and computational approaches. On the experimental side, several techniques have been used to measure structural changes that reflect the LLPT. For example, neutron scattering has been applied to the supercooled liquid of a Zr-Cu-Al-Ag alloy[17], while Raman spectroscopy has been used to study ionic liquids[18] or aqueous solutions[19,20]. However, the results obtained from experiments on aqueous solutions, which prevent rapid crystallization, cannot be straightforwardly extrapolated to water[21]. On amorphous ice, X-ray experiments have shown results consistent with a first-order phase transition[22,23]. More recently, Kim et al. conducted experiments on micro-sized liquid water droplets[24–26] and bulk[16]. Their results show a sudden change in the structure factor at one order of magnitude shorter times than subsequent crystallization, which is consistent with LLPT for temperatures around (205 ± 10) K and pressures between 1 atm and 350 MPa[16], and the presence of an LLCP at positive pressure[16,24,27].

On the computational side, different models support the LLCP in water, either rigid or flexible. The rigid ST2[8], has been rigorously proven to have an LLPT[15,28–32], as well as TIP4P/2005[33,34], TIP4P/Ice[33–36], TIP4P[37], and patchy models[38,39]. Flexible models, such as the polarizable WAIL[40] and the iAMOEBA[41], which employs point multipole electro-

[a)]Current address: Laboratoire de Biochimie Théorique, UPR 9080 CNRS, 13 rue Pierre et Marie Curie, 75005 Paris, France
[b)]On leave: Max Planck Institute for the Physics of Complex Systems, Nöthnitzer Straße 38, Dresden, 01187, Germany

statics and an approximate description of electronic polarizability, with up to three-body terms[42], also have an LLCP.

Other models that display LLCP and include many-body interactions to describe the cooperative nature of hydrogen bonding are the coarse-grained water monolayer with up to five-body interactions[43], the EB3B with up to three-body interactions[44,45] using the TIP4P/2005[46] as two-body reference, the coarse-grained machine-learned ML-BOP[14,47], with up to four-body interactions[48], and, just released, the DNN@MB-pol model[49] that is a machine-learning surrogate of the MB-pol, a model with mean-field-like representations of many-body electrostatic interactions integrated with machine-learned representations of short-range quantum-mechanical effects[50].

Furthermore, the phenomenological two-states equation of state (TSEOS) fits remarkably well to several water models[40,51–53] by assuming the LLCP hypothesis[54]. Although the TSEOS fitting method does not constitute definite proof, it is beneficial if simulation data is not available at the hypothesized critical point, as it shows that the model is at least consistent with the presence of an LLCP.

Simple models can help us understand the physical mechanisms that lead to the LLCP. For example, the role of HB cooperativity, or spatial correlation, has been emphasized both in continuous[55,56] and two-states model[11,57–61]. Based on available experimental data, cooperative models[11,62] have predicted the LLCP at positive pressure.

On the other hand, commonly used water models, such as SPC/E or mW, do not display the LLCP, showing no necessary relation with the water anomalies[63,64]. In other models, e.g., the TIP4P/2005, severe finite-size effects are an issue[65], and extremely long simulations of more than 50 μs for 1000 molecules are necessary to obtain well-converged density distributions for deeply supercooled water[33]. Despite their differences in the supercooled water, these models qualitatively reproduce the experiments around ambient conditions. Hence, the challenge to understanding the metastable water phase diagram is to explore a model that can a) *quantitatively* reproduce water thermodynamics over a broad range of temperatures and pressures, b) do it for system sizes large enough to perform the necessary finite-size scaling analysis and c) perform the calculations at an accessible computational cost.

In this study, we examine the phase diagram of metastable liquid water for the CVF model, introduced in Ref. [66] and defined in Appendix A, which is exceptionally accurate in replicating the experimental data of water's density and response functions in a broad region of thermodynamic conditions. Precisely, the model's quantitative agreement with the experiments is demonstrated in Ref. [66] by explicitly comparing the calculated density, isobaric specific heat, isobaric thermal expansivity, isothermal compressibility, and the locus of the temperatures of maximum density (TMD) and other loci associated with the response functions with the available experimental data. The accuracy is quantitative around room temperature for more than 60 K at 1 atm and around 40 K up to 50 MPa. Although the agreement of the density is quantitative on a broader thermodynamic region, the response functions become qualitative outside this range. Nevertheless, the model offers precise predictions over an unprecedented wide range of temperatures and pressures for water's equation of state and thermodynamic response functions. Therefore, it is interesting to study its calculations for metastable liquid water.

Although the model can be defined to include crystal phases and polymorphism[67,68], here we consider a formulation that focuses on the hydrogen bonds (HBs)—the fast degrees of freedom of the system—and coarse grains the molecular coordinates, which are the slow degrees of freedom that equilibrate over the time scales needed for crystallization. Combined with the Monte Carlo method described below, this formulation includes only fluid or amorphous configurations. Therefore, the model leverages the time-scale separation—observed in experiments[16] and atomistic simulations[36] of supercooled water between liquid-phase equilibration and homogeneous nucleation—to avoid crystallization while focusing on the liquid phase. This feature is advantageous for studying metastable liquid water, as it allows efficient sampling of the free energy landscape associated with fluid phases.

Additionally, the model's simple definition enables the use of advanced numerical techniques, avoiding dynamical slowing down near critical points or approaching a glassy state, which is typically found in supercooled water. One of these techniques, based on percolation mapping, is briefly described at the end of section II A. Consequently, the CVF model emerges as an intriguing candidate to explore the phase diagram of metastable water in regions currently inaccessible to experiments.

Another compelling advantage of the CVF model is that it allows for efficient equilibration of free energy calculations for systems up to 10 million molecules using common GPUs[69]. All these features are crucial for analyzing metastable water because small-size effects, glassiness, and crystallization typically hamper similar studies.

Using a state-of-the-art procedure[33,40,43,70], we equilibrate the metastable water under extreme conditions and systematically study finite but large systems. This allows us to extrapolate the thermodynamic behavior in the infinite-system limit, following the finite-size scaling theory, and demonstrate, with great accuracy, the existence of the LLCP for the model in the thermodynamic limit. We show that the LLCP belongs to the 3D Ising universality class, corroborating the thermodynamic consistency of the result. We compare our prediction with other models, finding similarities that suggest that the hydrogen bond network can develop significant cooperative fluctuations at scales relevant to nanotechnology applications and biological systems.

II. MONTE CARLO METHOD

A. Large-scale Monte Carlo free energy calculations for metastable bulk water

We perform Monte Carlo (MC) calculations of the free energy of the CVF water model in 3D with parameters able to reproduce quantitatively the equation of state of liquid water

over a temperature range of approximately 60 degrees around ambient conditions at atmospheric pressure and about 40 degrees up to 50 MPa[66]. The CVF model is defined in Appendix A. We consider a constant number of molecules N, pressure P, and temperature T in a variable cubic volume $V_{\rm Tot}$ with periodic boundary conditions.

We calculate the equation of state along isobars in the range of -540 MPa to 260 MPa, separated by intervals $\Delta P \leq 50$ MPa. The range of temperatures is 187 K to 470 K, with simulated thermodynamic points at variable resolution, $0.014\ {\rm K} \leq \Delta T \leq 14$ K, depending on the region of interest. The data presented here include results for systems of up to N =32,768 water molecules. We tested on several selected state points (not shown) that thermodynamic quantities calculated for N =262,144 are statistically similar to those for N =32,768 within our numerical precision but require roughly ten times longer to compute.

We apply the sequential annealing protocol along isobars, starting at high T and lowering the temperature in stages, allowing the system to equilibrate at each stage. We check the equilibration by verifying the validity of the fluctuation relation for the response functions defined in the following. We collect data by averaging over 10^4 - 10^5 MC steps after equilibration, corresponding to 10^3 - 10^4 independent configurations depending on the state point.

For N =32,768, we apply the Metropolis algorithm at temperatures $T \geq 215$ K. At lower temperatures, we use the Swendsen-Wang cluster algorithm[71,72] based on the site-bond correlated percolation applied to water[73]. This approach allows us to overcome the slowing down due to the approaching of the glassy state[74] that characterizes water dynamics at these values of T and P[29,31,75]. We optimize the performance of our simulations by implementing parallelization in GPUs using CUDA[69].

B. Monte Carlo calculations in the critical region

As described in the section III, we estimate the loci in the (T,P) plane where the response functions of metastable water have maxima and verify if, in the region where they converge, the fluctuations exhibit the expected finite-size behavior near a critical point. To achieve this, we compare calculations for systems with N up to 4,096 water molecules. These sizes were selected to ensure that the coexisting HDL and LDL states could transition frequently within reasonable simulation time. Larger systems exhibit single transitions from HDL to LDL, consistent with the expected exponential decrease of the transition rate as the free energy barrier between the phases increases.

We apply the sequential annealing protocol starting at $T =$ 270 K at each P and N, using the Wolff cluster algorithm[71,76]. We adapt the temperature resolution to the T-derivative of the calculated quantity, ranging from $\Delta T = 0.014$ K to 14 K. We observe that the Wolff algorithm's implementation on CPUs outperforms Swendsen-Wang, particularly for small N. After a preliminary isobaric scan, we select the T for each N with the most frequent transitions between the HDL and LDL states and adjust the simulation time. We find that the time necessary to observe multiple HDL-LDL transitions rapidly increases with N, ranging from 10^5 to 10^8 MC steps for N going from 512 to 4,096 (see Supplementary Information, Table S1). For N =4,096, we observe coexistence only for $P \geq 110$ MPa.

C. LLCP and universality class analysis

To rigorously prove the presence of an LLCP, we need to identify the correct order parameter (o. p.) that describes the phase transition. In fluid-fluid phase transitions, the critical point belongs to the 3D Ising universality class with a *mixed-field* o. p. that combines the number density with the energy density to account for the lack of symmetry in the critical density distribution[70,77]. Therefore, definitive proof that the CVF model displays an LLCP is that the fluctuations of the correct o. p. behave in a manner consistent with those of the magnetization of the 3D Ising model at its critical point, as shown already for soft-core isotropic anomalous fluids[78], rigid[31,33], and flexible[40] water models, as well as the Stillinger-Weber model for silicon[79]. The same approach has also been used to show that the confined water monolayer has an LLCP belonging to the 2D Ising universality class[43].

In the NPT-ensemble, based on finite-size scaling theory for density-driven fluid-fluid phase transitions[77], the o. p. is $M(s) \equiv \bar{\rho} + s\bar{e}$, where $\bar{\rho}$ and $\bar{e}$ are dimensionless density and energy, respectively, and s is the so-called *mixing parameter*. This linear combination symmetrizes the probability distribution of the coexisting states that for water at the LLCP would correspond to HDL and LDL phases[43,73].

We use the histogram reweighting method[43,80] to find the critical temperature T_C, critical pressure P_C, and s values that allow us to fit the fluctuations of M with those expected for the Ising 3D critical point. To do this, we calculate by MC the histogram $H_i(T_i,P_i;e,\rho)$ of visited configurations with given molar energy e and density ρ for state points (T_i, P_i) within the critical region. By normalizing H_i, we provide a finite-size (numerical) approximation of the probability density distribution $Q(e,\rho)$ of states with given (e,ρ) for the system in the thermodynamic limit. We then combine a set of H_i by the histogram reweighting method to calculate $H(T,P;e,\rho)$ for any (T,P) near (T_i, P_i)[43].

We optimize T_C, P_C, and s based on $H(T,P;e,\rho)$ in the critical region to ensure that the integral of $H(T_C,P_C;e,\rho)$ over (e,ρ) corresponding to the same $M(s)$—i.e., $H(T_C,P_C;M(s))$—has a bimodal distribution centered around a value that we indicate as $M_C(s)$. Then, as discussed in Appendix B, we determine a rescaled version of $M(s)$, $x = x(s)$ with zero mean and unit variance, with a probability density distribution $Q(x)$ at (T_C,P_C) approximating that of the 3D Ising model o. p. m_I at criticality, $Q_3(m_I)$. We iterate the process and selection of T_C, P_C, and s to minimize the difference between Q and Q_3.

III. RESULTS

A. Density, enthalpy, and HB network.

At temperatures below the liquid-gas (LG) spinodal, along isobars, the model displays a temperature of maximum density (TMD) (Fig. 1a). We use the highest temperatures before abrupt changes toward gas values of the isobaric density ρ and other thermodynamics quantities as our numerical approximation of the LG spinodal at a fixed system size. For the sake of simplicity, we will refer to these estimates as LG spinodal, although they are only a lower-T proxy of it.

The model's TMD is in quantitative agreement with the available experimental data for water as shown in Ref.[66] (see also Fig. S2). Decreasing the temperature below the TMD leads to a decrease in the isobaric density ρ toward a temperature of minimum density (TminD), with a weak increase below TminD (Fig. 1a). Experiments under confinement, inhibiting water crystallization, show similar behavior, as recently summarized in Ref.[81].

The temperature of the large variation in ρ displays a pronounced P-dependence. Increasing P approaching $P_{\rm TMD}^{\rm Max} \simeq$180 MPa, the jump toward the minimum is sharper compared to low P, and the maximum becomes flatter. Above $P_{\rm TMD}^{\rm Max}$, the density becomes monotonically decreasing for increasing T, and the TMD ends[66], in agreement with the experiments[81,82]. The value of $P_{\rm TMD}^{\rm Max}$ can be calculated in the model, in its simplified assumption for the volume Eq. A4, which implies that the liquid compressibility does not change with P (Fig. S1).

The P-dependence of the change in ρ could be apparently consistent with the LLPC scenario at negative P[83]. However, a similar behavior, without any discontinuity, is also predicted by the singularity-free scenario[9,11,55].

Therefore, we analyze the enthalpy per molecule h and find variations at any P (Fig. 1b). Opposite to density changes, the variation in h is sharper at lower P and smoother at higher P, with an amplitude of about 5 kJ/mol that is approximately independent of P in the range of pressures we consider. Also, in contrast with ρ, the temperature of maximum variation of h, between 197 K and 205 K, has a weaker pressure dependence. Because h depends both on the density and the HB interactions, the mismatch between the P-dependence of enthalpy and density demonstrates that the HB network and its rearrangement control the most significant variation in h.

On the other hand, also $\rho \equiv V_{\rm Tot}/N$ depends on the number of HBs, $N_{\rm HB}$, Eq. A4. For decreasing T, $N_{\rm HB}$ rapidly increases at high P up to $P_{\rm TMD}^{\rm Max}$, and displays a smoother increase at low P (Fig. 1c). At constant T, $N_{\rm HB}$ decreases for increasing P consistent with the experiments[81].

At high T, $N_{\rm HB}$ converges toward a low average value. Around atmospheric pressure, this value is close to the lowest possible $\approx$20%, corresponding to the stochastic probability of having two nearby water molecules with one of their H atoms in between (Appendix A).

At low temperatures and $P > P_{\rm TMD}^{\rm Max}$, above the TMD, $N_{\rm HB}$ decreases because of the ρ-increase that breaks the tetrahedral HB network. This is consistent with the known phenomenon

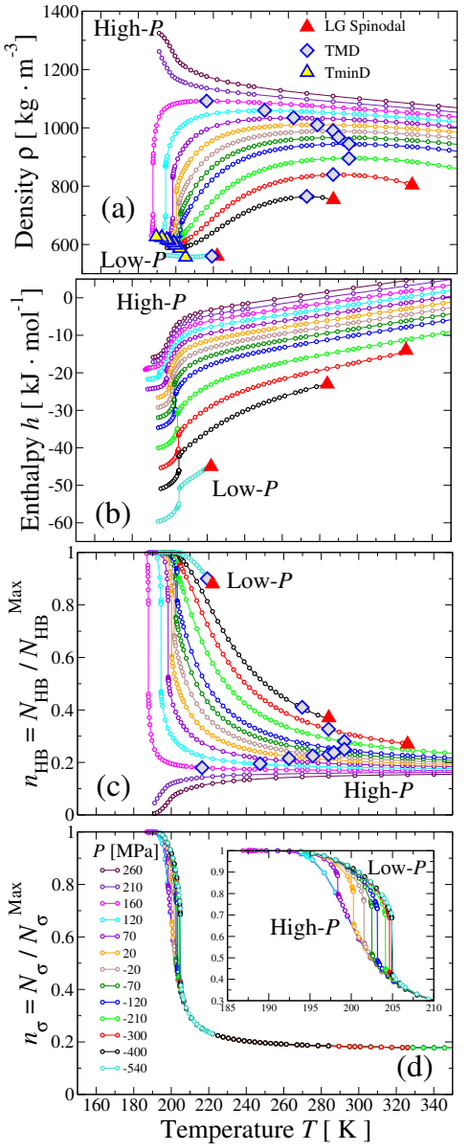

FIG. 1. **Temperature dependence of CVF water thermodynamic quantities along isobars below 260 MPa.** In all the panels, circles are MC calculations for N =32,768 water molecules, lines are guides to the eyes, colors correspond to different pressures indicated in the legend of the bottom panel (from −540 MPa to 260 MPa), grey diamonds mark the TMD, and red triangles are our finite-size numerical estimates of the LG spinodal as the highest temperature along each isobar before the abrupt transition of ρ and h (in panels a and b, respectively) to values below the reported scales. **(a)** For each $P \le P_{\rm TMD}^{\rm Max} \simeq$ 180 MPa (see also Fig. S1), the density ρ, expressed in kg/m^3, has a maximum (TMD) and a minimum (TminD, yellow triangles). **(b)** The enthalpy per molecule h, expressed in kJ/mol, decreases monotonically for decreasing T, with a large variation around a temperature weakly dependent of P. **(c)** The normalized number of HBs, $n_{\rm HB}$ with $N_{\rm HB}^{\rm Max} \equiv 2N$, at constant T decreases for increasing P. Upon isobaric cooling, it increases for P up to $P_{\rm TMD}^{\rm Max}$ and decreases for higher P. The increase is sharper for P approaching $P_{\rm TMD}^{\rm Max}$. **(d)** The number of cooperative HB bonds n_σ, normalized with respect to their maximum value $N_\sigma^{\rm Max}$, increases at low T with a variation that is smoother at higher P. Inset: The detail around the variation reveals that this change correlates with the enthalpy change in (b).

of melting ice by pressurization due to the change of slope of the melting temperature around 200 MPa[82]. These high pressures also mark the onset of the ice polymorphism, leading to the formation of interpenetrating HB networks at larger pressures[84,85].

At low temperatures below $P_{\rm TMD}^{\rm Max}$, $N_{\rm HB}$ saturates to two HBs per molecule ($N_{\rm HB}^{\rm Max} \equiv 2N$), i.e., every water molecule is participating in four HBs. However, the changes of $N_{\rm HB}$ at low pressure are not discontinuous as in the enthalpy, showing that the contribution to h coming from HB cooperativity is relevant (Appendix A).

In particular, N_σ is the number of locally cooperative, or tetrahedrally arranged, HBs (Appendix A). It displays a rapid increase that is sharper at low pressure and smoother for $P > 70$ MPa (Fig. 1d). Unlike $N_{\rm HB}$, the change in N_σ occurs between 197 K and 205 K, with a weak dependence on P, correlating with the variation in h.

Therefore, the significant decrease of h is associated with the cooperative contribution, resulting from an extensive structural rearrangement of the HBs towards a more tetrahedral configuration. However, this reorganization implies only a minor change in ρ at low pressure, as it occurs when the number $N_{\rm HB}$ of HBs is almost saturated.

On the other hand, by increasing P toward $P_{\rm TMD}^{\rm Max}$, a large amount of HBs form at low T, where the many-body interaction is already relevant. Therefore, at high P, the effect of $N_{\rm HB}$ on the density is significant and collective, as expected at a critical phase transition.

B. Isobaric specific heat.

To test whether the observed thermodynamic behavior is consistent with criticality, we calculate the response functions C_P, K_T, and α_P and study if they diverge at the hypothesized LLCP. We find sharp maxima in $C_P \equiv N\left(\langle h^2\rangle - \langle h\rangle^2\right)/k_B T^2$ at any pressure P and low T with an apparent divergence at -70 MPa$\leq P \leq 20$ MPa within our numerical resolution (Fig. 2a).

For pressures below 20 MPa, the locus of the maxima of C_P depends weakly on P, occurring around 200 K, in the range of T where h and N_σ have significant changes (Fig. 2b). For pressures $P > 20$ MPa, the sharp maxima decrease in intensity and move toward lower temperatures. This behavior would be consistent with an LLPT line with a negative slope in (T,P) ending in an LLCP where $C_P(T)$ apparently diverges (Fig. 2b).

Between the TMD line, that coincides within the statistical error with the experimental data as reported in Fig. 2b, 3b, and 4b, and the LG spinodal, C_P has isobaric minima (Fig. 2a, inset). Between 0 and 50 MPa, the minima agree, within the statistical error, with the experimental data, as reported in Fig. 2b and discussed in Ref.[66].

As P decreases, the locus $C_P^{\rm min}(P)$ is between the TMD line and the lower-T numerical (finite-size) proxy for the LG spinodal never coinciding with the latter (Fig. 2b). The TMD line and the LG spinodal do not intersect, which is consistent with the monotonicity of the spinodal pressure versus temperature.

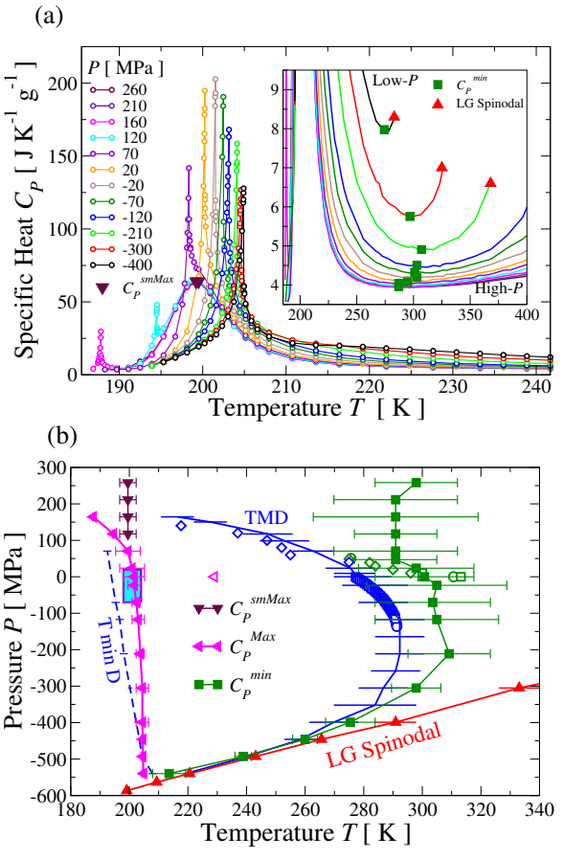

FIG. 2. **The isobaric specific heat has maxima at low temperatures with apparent divergence below 200 MPa.** In all panels, the MC calculations are for N =32,768 water molecules, dark-green squares mark specific heat minima $C_P^{\rm min}(P)$, indigo triangles mark smooth maxima $C_P^{\rm smMax}(P)$, and red triangles are the finite C_P value calculated at the highest T within our numerical resolution before the divergence at the LG spinodal. **(a)** C_P, in J/(gK), as a function of T, in K, along isobars from -400 MPa to 260 MPa (with colors as indicated in the legend). For clarity, we show only a selection of results from the fluctuation relation. Circles are the calculations, and lines are guides to the eyes. Sharp maxima, $C_P^{\rm Max}(P)$, occur at any P, achieving higher values between -70 MPa and 20 MPa. For $P \geq 120$ MPa, we find also smooth maxima, $C_P^{\rm smMax}(P)$, almost P-independent. Inset: The details of the same data, represented as lines for clarity, at high T around the $C_P^{\rm min}(P)$. C_P diverges at temperatures just above those marked by the red triangles. **(b)** In the (T,P) thermodynamic plane, the locus of $C_P^{\rm min}(P)$ approaches from lower T the numerical (finite-size) proxy for the LG spinodal but never coincides with it, at $P < 0$, before turning into the locus of $C_P^{\rm Max}(P)$ (magenta left triangles), where the TMD (blue solid) line turns into the TminD (blue dashed) line. At high P, the locus of $C_P^{\rm smMax}(P)$ departs from that of $C_P^{\rm Max}(P)$ near the state points where C_P apparently diverges (cyan region). The TMD line and the $C_P^{\rm min}(P)$ locus are in quantitative agreement within the statistical error with the experimental data above the homogenous nucleation temperature T_h[81] (not shown) for the TMD (blue diamonds[82]; blue squares[86]; blue circles[87]), and $C_P^{\rm min}(P)$ (dark-green diamonds[88]; dark-green circles[89]; dark-green squares[90]), respectively. Below T_h, the agreement with the $C_P^{\rm Max}(P)$ from experiments at atmospheric pressure (magenta open triangle[91]) is only qualitative, calling for further investigation.

The LG spinodal should otherwise be reentrant in case of intersection with the TMD[92].

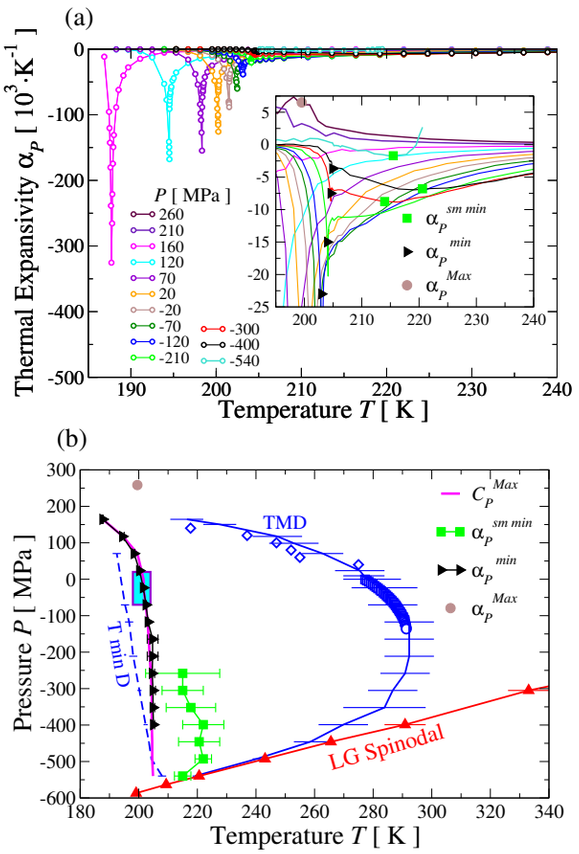

FIG. 3. **The isobaric thermal expansivity grows negative below the TMD line with extrema along the $C_P^{\mathrm{Max}}(P)$ locus.** In all panels, the MC calculations are for N =32,768, black triangles mark sharp minima $\alpha_P^{\mathrm{min}}(P)$, green squares mark smooth minima $\alpha_P^{\mathrm{sm\ min}}(P)$, brown circle marks a maximum $\alpha_P^{\mathrm{Max}}(P)$ at 260 MPa. **(a)** α_P, in K^{-1}, as a function of T, in K, along isobars from -540 MPa to 260 MPa (with colors as indicated in the legend). For clarity, we show only the results from the fluctuation relation (circles) for a selection of the calculated isobars. Lines are guides to the eyes. The expansivity has minima, $\alpha_P^{\mathrm{min}}(P)$, that are sharp and strong at high $P > 0$. They become weaker as P decreases. Inset: The same data as in the main panel, represented as lines for clarity, around the $\alpha_P^{\mathrm{sm\ min}}(P)$, for T above the $\alpha_P^{\mathrm{min}}(P)$. The sharp minima disappear for $P < -400$ MPa, while, for $P \leq -250$ MPa, the expansivity develops the smooth minima at higher-T. We find a maximum $\alpha_P^{\mathrm{Max}}(P)$ at 260 MPa. **(b)** The locus of $\alpha_P^{\mathrm{min}}(P)$ follows the locus of $C_P^{\mathrm{Max}}(P)$ (magenta line), crossing the state points where C_P apparently diverges (cyan region). The locus of $\alpha_P^{\mathrm{sm\ min}}(P)$ converges at low P toward the $C_P^{\mathrm{Max}}(P)$ line and crosses the TMD (blue solid) line where it turns into the TminD (blue dashed) line, approaching but never touching the LG spinodal (red line). Experimental data for the TMD line are as in Fig.2b.

The locus $C_P^{\mathrm{min}}(P)$ crosses the TMD line where the minima in C_P turn into maxima $C_P^{\mathrm{Max}}(P)$ and, at the same time, the TMD line turns into the TminD line, as expected for thermodynamic consistency. This is due to the relation[43]

$$\left(\frac{\partial C_P}{\partial P}\right)_{T,\mathrm{TMD}} = T\left(\frac{\partial P}{\partial T}\right)_{\mathrm{TMD}}\left(\frac{\partial^2 V}{\partial P \partial T}\right)_{\mathrm{TMD}} \qquad (1)$$

indicating that the TMD line has a vanishing T-derivative, as in a turning point, in the (T,P) plane, $(\partial P/\partial T)_{\mathrm{TMD}} = 0$, when it intersects the locus of C_P extrema and they are independent of P, i.e., $(\partial C_P/\partial P)_{T,\mathrm{TMD}} = 0$[43,87,93].

At $P > 70$ MPa, we find that C_P develops smooth isobaric maxima $C_P^{\mathrm{smMax}}(P)$ at intermediate T, between the loci of $C_P^{\mathrm{Max}}(P)$ and $C_P^{\mathrm{min}}(P)$ and these maxima are independent of P (Fig. 2). The following explains that the locus $C_P^{\mathrm{smMax}}(P)$ is necessary to maintain thermodynamic plausibility and data consistency. As ρ increases, water loses its anomalies[94]. As density always increases with increasing pressure, a similar relationship holds with P. Hence, the locus $C_P^{\mathrm{min}}(P)$ must end at a sufficiently large pressure P_{Max} above which water is no longer anomalous. Consequently, there are only two possible thermodynamically consistent cases:

I. The locus $C_P^{\mathrm{min}}(P)$ has a turning point at a limiting pressure P_{Max}, merging into a locus of maxima of C_P occurring at lower temperatures and crossing the TMD line. For Eq. (1), because the maxima $C_P^{\mathrm{smMax}}(P)$ are independent of P, the TMD line has zero slope in the (T,P) plane at the crossing point. Hence, the TMD line flattens out or has a turning point at the high-P crossing with the C_P extrema. Both possibilities are consistent with the experimental data. For example, in Ref.[81] the TMD flattens out in this region of the (T,P) plane, while a high-P TMD turning point has been extrapolated in Ref.[95] based on the experimental data. Therefore, both possibilities are consistent with our model's observations, as discussed above and in the next section, III C, for the isobaric thermal expansivity at high P.

II. The locus $C_P^{\mathrm{min}}(P)$ at the limiting pressure P_{Max} extends to zero temperature without a high-P turning point. There is no necessary crossing with TMD in this case as, for example, described in the singularity-free hypothesis[96]. However, in the singularity-free scenario, the C_P minimum occurs at a temperature lower than the TMD at ambient pressure. This is inconsistent with experimental data because the minimum of C_P at 1 atm occurs at a temperature higher than the TMD, as reported in Fig. 2. The alternative, with the locus of $C_P^{\mathrm{min}}(P)$ embedding the TMD for $P > 0$ would still be consistent with the analysis in Ref.[81] but would be inconsistent with the extrapolation from the experiments in Fig. 2.9 of Ref.[95] showing a turning point in TMD. This turning point implies a crossing with the locus of zero T-derivatives of α_P, and this, in turn, coincides with the locus of extrema in C_P, as discussed in the next section III C.

Hence, only Case I is thermodynamically plausible and consistent with all the experimental data interpretation or extrapolation. The detailed study of the high-P turning point of C_P

extrema and the TMD, although interesting, goes beyond the scope of the current work.

The two C_P maxima observed here are qualitatively different from those discovered by Mazza et al. for the water monolayer[97]. Consistent with experiments for a water monolayer[98], Mazza et al. found the two C_P maxima also at low pressures, approaching the LG spinodal. Here, instead, we find two maxima only at pressures above the possible critical region, as in experiments of confined water[99,100] and atomistic simulations of bulk water[53,101,102].

C. Isobaric thermal expansivity.

Next, we calculate the thermal expansivity, $\alpha_P \equiv (\langle VhN\rangle - \langle V\rangle\langle hN\rangle)/(k_B T^2\langle V\rangle)$, along isobars (Fig. 3a). We observe sharp minima, $\alpha_P^{\min}(P)$, along the $C_P^{\rm Max}(P)$ line, with decreasing intensity as the P reduces (Fig. 3b). At -210 MPa, α_P develops a shoulder at temperatures above the minimum (Fig. 3a, inset). As the pressure decreases, the shoulder becomes a smooth minimum $\alpha_P^{\rm sm\ min}(P)$. For -400 MPa $\leq P \leq -250$ MPa, α_P has a primary minimum, $\alpha_P^{\rm sm\ min}(P)$, at higher T and a secondary minimum, $\alpha_P^{\min}(P)$, at lower T.

The fact that both α_P, proportional to the cross-fluctuations of entropy and volume[105], and C_P, proportional to the fluctuations of entropy[105], have extrema along the same locus in the plane (T,P) indicates that at these specific state points there is the most extensive rearrangement of the HB network towards a more tetrahedral ordering. This is in agreement with the N_σ significant variation observed in Fig.1 d. Hence, the sharp minima in α_P correspond to maxima in the structural rearrangement of the HB network.

The smooth minima in α_P at negative P indicate that the HB ordering can occur progressively at intermediate T. The $\alpha_P^{\rm sm\ min}(P)$ line correlates in T with the largest variation of the gradual increase of $N_{\rm HB}$ at low P (Fig.1c).

At higher and positive P, the energy gain of the HBs can overcome their high enthalpy cost, due to the local volume increase, only at low enough T, inducing a merging, within the error bar, of the smooth and the sharp minima. This should occur at the $C_P^{\rm Max}(P)$ line, where N_σ and $N_{\rm HB}$ increase together at high P, as suggested by our calculations.

Also, all these observations are consistent with the mean-field results showing that α_P is proportional to the isobaric T-derivative of the probability of forming HBs, apart from a term that is relevant only near the LG spinodal[105]. Hence, it correlates with the HB-network structural changes marked by the derivatives of N_σ and $N_{\rm HB}$.

It is interesting to note that our results indicate that the positions of the two minima, $\alpha_P^{\rm sm\ min}(P)$ and $\alpha_P^{\min}(P)$, become identical when they approach the LG spinodal. The position of $\alpha_P^{\rm sm\ min}(P)$ approaches the LG spinodal and the TMD line before turning towards the $\alpha_P^{\min}(P)$ position where the TMD line and the TminD line merge (Fig. 3b). This is consistent with the thermodynamic relation

$$\left(\frac{\partial \alpha_P}{\partial T}\right)_{P,\,\rm TMD} = -\frac{1}{V}\left(\frac{\partial P}{\partial T}\right)_{\rm TMD}\left(\frac{\partial^2 V}{\partial P \partial T}\right)_{\rm TMD}, \qquad (2)$$

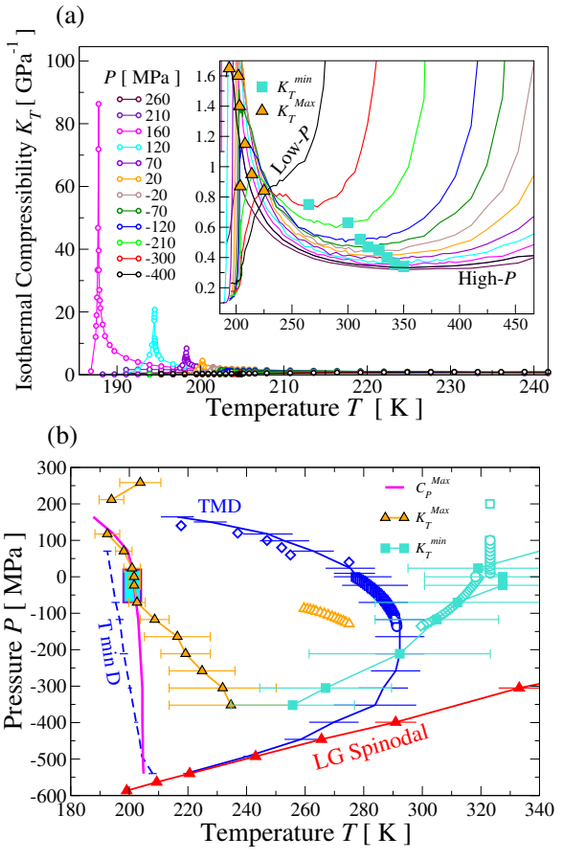

FIG. 4. **The isothermal compressibility has maxima below the TMD line merging the $C_P^{\rm Max}(P)$ line where C_P apparently diverges.** In all panels, the MC calculations are for N =32,768, solid orange upper triangles and solid turquoise squares mark maxima $K_T^{\rm Max}(P)$ and minima $K_T^{\min}(P)$, respectively. **(a)** K_T, in GPa^{-1}, as a function of T, in K, along isobars from -400 MPa to 260 MPa (with colors as indicated in the legend). For clarity, we show only the results (circles) from the fluctuation relation for a selection of the calculated isobars. Lines are guides to the eyes. The maxima $K_T^{\rm Max}(P)$ rapidly decrease upon decreasing $P < 200$ MPa. Inset: The same data as in the main panel, represented as lines for clarity, showing the convergence of the $K_T^{\rm Max}(P)$ and the minima $K_T^{\min}(P)$. We also show the two maxima above 200 MPa at $\simeq$ 187 K and 202 K. **(b)** The $K_T^{\rm Max}(P)$ line converges to the (cyan) region where C_P apparently diverges and merges with the $C_P^{\rm Max}(P)$ (magenta) line. The locus of $K_T^{\min}(P)$ crosses the TMD (blue) line in its turning point (point of maximum slope), in quantitative agreement with the available experimental data above the TMD (turquoise squares[103]; turquoise circles[104]; turquoise diamonds [87]). The agreement with the experimental data for $K_T^{\rm Max}(P)$ in stretched water below the TMD (orange empty triangles[87]) is only qualitative and should be further investigated. We find $K_T^{\rm Max}(P)$ at pressures above 200 MPa. Extrema in K_T are related to extrema in α_P as regulated by Eq. (4). We find $K_T^{\rm Max}(P)$ also at pressures above 200 MPa.

showing that α_P has zero T-derivative, as in a minimum, if it crosses the TMD line where the slope is zero, i.e., where it turns into the TminD line.

Our calculations along isobars in the range 160 MPa $< P <$

200 MPa show that $\alpha_P(T)$ flattens out around 180 K (Fig. S3), where C_P has a smooth maximum. Hence, for Eq. (2), the TMD line has a zero slope in the (T,P) plane at the crossing point, as discussed in case I in section III B, consistent with the two experimental scenarios proposed in Ref.[81] and in Fig. 2.9 of Ref.[95].

The Eq. (2) also holds for a maximum in α_P. We can observe potential maxima at -540 MPa around 205 K (Inset Fig.3a) and at approximately the same temperature but at very high pressure (260 MPa). This suggests that, as observed for the other response functions, the locations of the extremes should trend towards high pressure and high temperature and then converge towards the region where C_P seems to diverge, forming a closed region in the (T,P) plane. Further investigation beyond the scope of the present work will be required to understand this feature.

D. Isothermal compressibility.

Finally, we calculate the isothermal compressibility, $K_T \equiv \langle V^2\rangle/k_BT\langle V\rangle$, along isobars (Fig. 4a). We observe that K_T has maxima, $K_T^{\rm Max}(P)$, that in the (T,P) plane converge toward the extrema of C_P and α_P (Fig. 4b). All the extrema of the three response functions merge in the region where C_P apparently diverges and follow each other at higher P, as it would be expected along a first-order LLPT with a negative slope in the (T,P) plane ending in an LLCP.

As the pressure decreases, the maxima $K_T^{\rm Max}(P)$ decrease and turn into minima, $K_T^{\rm min}(P)$. These minima occur at increasing temperatures with increasing pressure above -350 MPa and cross the TMD line at its turning point, in quantitative agreement with the available experimental data reported in Fig. 4b. As discussed in Refs.[43,87,93], this is a consequence of the thermodynamic relation[43]

$$\left(\frac{\partial K_T}{\partial T}\right)_{P,\,\rm TMD} = \frac{1}{V}\frac{(\partial^2 V/\partial T^2)_{\rm TMD}}{(\partial P/\partial T)_{\rm TMD}} \qquad (3)$$

indicating that, at the TMD line, K_T has a zero T-derivative along isobars when the TMD line has an infinite slope. At pressures above 200 MPa, we find another branch of the locus of $K_T^{\rm Max}(P)$, as expected for thermodynamic consistency[38,106].

We observe that our calculations recover, within the error bars, the thermodynamic relation

$$\left(\frac{\partial \alpha_P}{\partial P}\right)_T = -\left(\frac{\partial K_T}{\partial T}\right)_P \qquad (4)$$

indicating that the extrema of K_T along isobars correspond to state points where α_P is constant along isotherms. Consequently, we find that α_P, calculated at close pressures, has crossing temperatures coinciding with the loci of extrema of K_T (Fig. S4).

E. Finite size analysis for the LLPT and the LLCP

The results in the previous sections are consistent with an LDL-HDL phase separation in finite systems. We perform a finite-size scale analysis to demonstrate the occurrence of the LLCP in the thermodynamic limit and estimate its universality class.

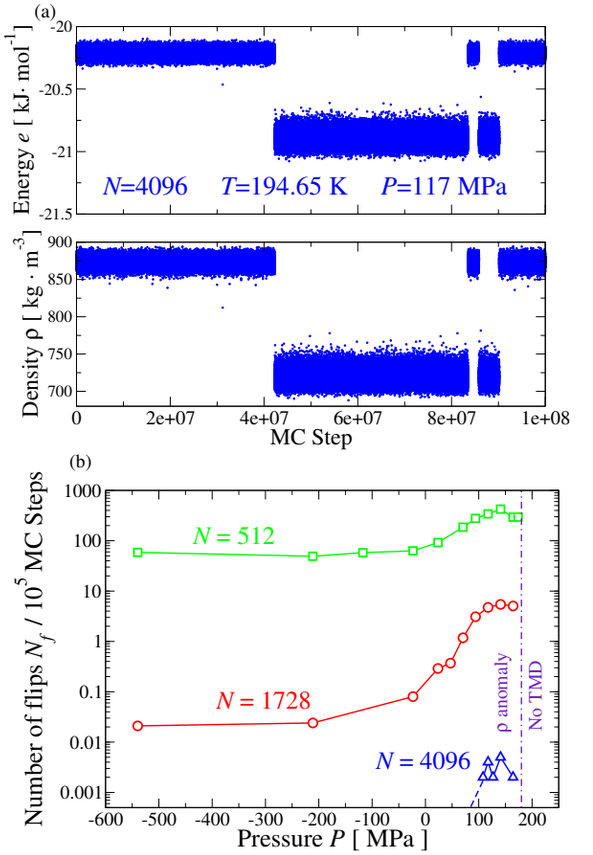

FIG. 5. **Correlated flipping in energy and density between HDL-like and LDL-like states. (a)** Sequence of (top panel) molar energy e, in kJ/mol, and (bottom panel) density ρ, in kg/m^3 for the configurations generated by the MC algorithm for a system with N =4,096 water molecules at T = 194.65 K, and P = 117 MPa. We observe four correlated flips between states with high (e,ρ) and states with low (e,ρ), as between HDL and LDL, respectively. **(b)** Number N_f of flips, within 10^5 MC steps, between high-(e,ρ) and low-(e,ρ) states at fixed N, for N =512 (green squares), 1,728 (red circles), and 4,096 (blue triangles), as a function of P, in MPa, along the (T,P) locus where the maxima in C_P, α_P, and K_T converge. Continuous lines are guides for the eyes. For N =4,096 water molecules, we do not observe any switching below 110 MPa within 10^8 MC steps (blue dashed line). The purple dot-dashed line indicates the pressure $P_{\rm TMD}^{\rm Max} \simeq 180$ MPa above which the model displays no density anomaly (maximum P of the TMD line, Fig. S1), consistent with the experiments[81,82].

The HDL-like and LDL-like states have high molar energy e and ρ, and low e and ρ, respectively. Consistently, we observe correlated switching between states with low and high values of e and ρ in our MC calculations (Fig.5a). These flips are consistent with a bimodal joint probability density distribution $Q(e,\rho)$, as in a phase coexistence.

At any number N of water molecules, the number N_f of

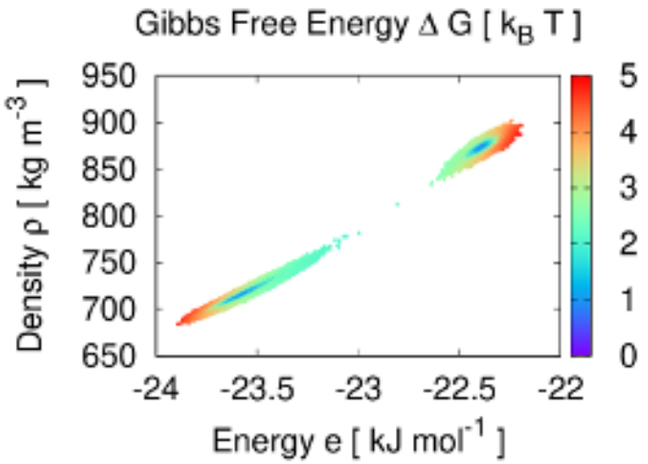

FIG. 6. **Gibbs free energy difference near the LLCP estimated for a finite system.** ΔG, in units of k_BT (colored-bar scale), for size N =4,096, as calculated with the histogram reweighting method, in the (e,ρ) plane, where the molar energy e is expressed in kJ/mol units and the density ρ in kg/m^3. The system samples with larger probability the two (blue) regions corresponding to LDL-like and HDL-like states at low-(e,ρ) and high-(e,ρ), respectively.

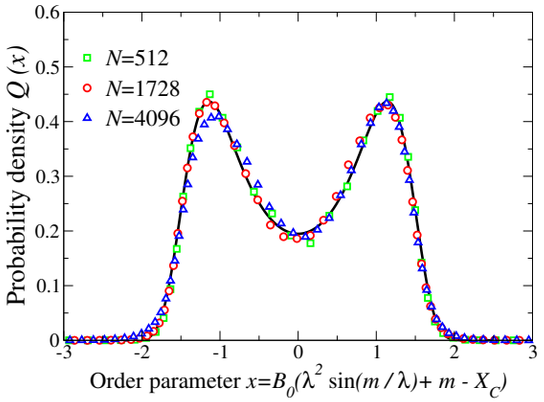

FIG. 7. **The water LLCP belongs to the 3D Ising universality class.** The rescaled o. p. $x(s)$, as defined in Appendix B, at the LLCP follows the 3D Ising critical probability density distribution Q_3 (continuous black line) in the thermodynamic limit. Symbols, as indicated in the legend, are for systems with N =512 (green squares), 1,728 (red circles), and 4,096 (blue triangles) water molecules. The critical parameters are reported in Table I.

TABLE I. Parameters adopted in Fig. 7. For each N, we adjust the critical parameters T_C, P_C, and s, as in section II C, to best fit the 3D Ising distribution Q_3.

N	T_C [K]	P_C [MPa]	s
512	202.7 ± 2.3	-141 ± 164	-36 ± 30
1,728	200.4 ± 3.4	59 ± 35	-76 ± 38
4,096	194.6 ± 1.0	117 ± 10	-142 ± 15

flips reaches a maximum around 150 MPa along the locus of maxima in C_P, α_P, and K_T. This pressure is close to the upper limit $P_{\rm TMD}^{\rm Max}$ beyond which water has no TMD both in our calculations (Fig. S1) and experiments[81,82] (Fig.5b).

As we increase N from 512 to 4,096, the value of $N_f(P)$ decreases by five orders of magnitude and eventually vanishes below 110 MPa within 10^8 MC steps (see Table S1). However, the flips still occur even for the largest N when $P \geq 110$ MPa. This is consistent with the expected behavior for state points near phase transitions in systems with a size smaller than the correlation length of the o. p. fluctuations. However, finite-size scaling theory allows one to extrapolate N-dependent critical parameters to the $N \to \infty$ limit near a critical point.

To calculate the N-dependent critical parameters, we resort to the histogram reweighting method (section II C). We estimate the free energy landscape $\Delta G(e,\rho)/k_BT = -\log(Q(e,\rho))$ near the LLCP for the largest system size (Fig. 6). Our analysis reveals two basins of attraction, one associated with a low-(e,ρ) state and the other with a high-(e,ρ) state, as expected at the LDL-HDL coexistence. These two basins are separated by a free-energy barrier of approximately $2k_BT$, which thermal fluctuations can easily overcome, consistent with the behavior near a critical point.

To localize the LLCP accurately and analyze its universality class in the thermodynamics limit, we estimate the mixing parameter s, which defines the o. p. $M(s)$ and its rescaled version $x(s)$, and the size-dependent critical temperature and pressure $(T_C(N), P_C(N))$, as described in section II C. Our results show that the $x(s)$ at the size-dependent LLCP follows the probability density distribution Q_3 of the 3D Ising critical point (Fig. 7). Therefore, we conclude that the LLCP belongs to the 3D Ising universality class in the thermodynamic limit.

In Table I, we indicate the parameters adopted in Fig. 7 for each N, finding strong finite-size effects. For N =512, we find fluctuations of x that follow Q_3 for a wide range of P and a limited range of T along the $C_P^{\rm Max}(P)$ line, as discussed in the next section. As N increases, the range of P at which $Q(x)$ is compatible with Q_3 becomes narrower, indicating that, for larger N, the region with critical fluctuations is smaller.

We analyze how T_C and P_C extrapolate to the thermodynamic limit. This analysis is crucial to determine whether the observed LLCP results from finite-size effects or is an intrinsic property of the model. According to the finite size scaling theory[77], the scaling laws of $T_C(N)$ and $P_C(N)$ are governed by the critical exponents of the universality class as

$$\begin{aligned} P_C(N) &= \mathscr{A}_P N^{-(\theta+1)/d\nu} + P_C \\ T_C(N) &= \mathscr{A}_T N^{-(\theta+1)/d\nu} + T_C \end{aligned} \tag{5}$$

where $\mathscr{A}_P$ and $\mathscr{A}_T$ are scaling constants, d is the dimensionality, ν the critical exponent controlling the divergence of the correlation length ξ, θ the correction to scaling, and $P_C \equiv P_C(N \to \infty)$ and $T_C \equiv T_C(N \to \infty)$ are the critical pressure and temperature, respectively, in the thermodynamic limit. For the 3D Ising model, it is $d = 3$, $\nu = 0.63$, and $\theta = 0.53$ [70].

By fitting the scaling laws of $P_C(N)$ and $T_C(N)$ to the three calculated LLCP(N), we find that $P_C(N)$ follows the expected

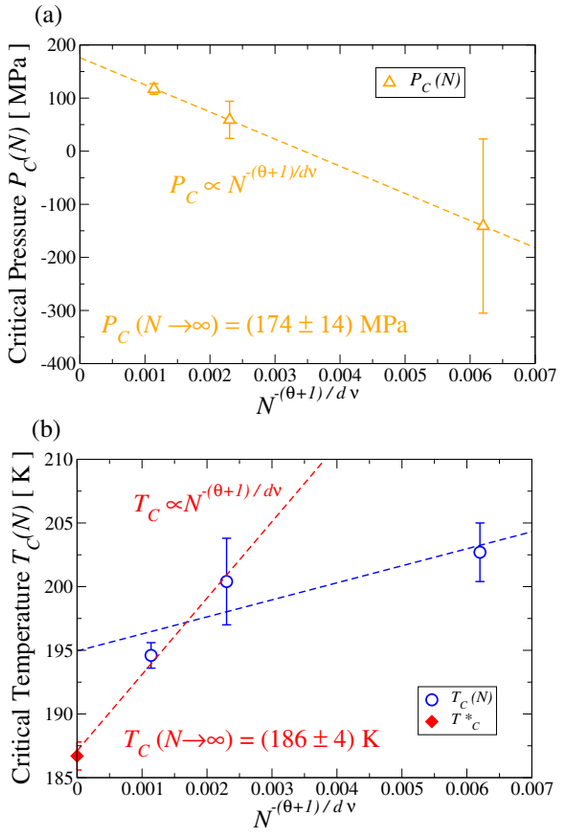

FIG. 8. **The scaling laws for the critical parameters are consistent with the 3D Ising critical exponents. (a)** $P_C(N)$, in MPa, follows the scaling law in Eq.(5) with 3D Ising critical exponents for the three sizes considered here, with $\mathscr{A}_P = (-5 \pm 3)10^5$ MPa and $P_C = (176 \pm 14)$ MPa. **(b)** $T_C(N)$ (blue circles), in K, deviates from the expected scaling law. However, by thermodynamic argument (see text), we can add the critical temperature $T_C(P_C^\infty)|_{\rm extrema} = (186.7 \pm 1.1)$ K (red diamond) corresponding to $C_P^{\rm Max}(P)$ at $P_C(N \to \infty)$. Excluding $T_C(N = 512)$ and adding $T_C(P_C^\infty)|_{\rm extrema}$, the calculated critical temperatures follow the 3D Ising critical scaling law in Eq.(5) with $\mathscr{A}_T = (6 \pm 1)10^3$ K and $T_C = (186 \pm 4)$ K (red dashed line).

power law (Fig. 8a), but $T_C(N)$ apparently does not (Fig. 8b). However, the correct dependence of $P_C(N)$, extrapolating to $P_C = (174 \pm 14)$ MPa, suggests that $T_C(N)$ has a stronger N-dependence than the critical pressure, inducing a significant deviation at the smallest size N =512.

To account for this, we observe that the LLCP in the thermodynamic limit must occur at a temperature $T_C(P_C^\infty)|_{\rm extrema}$ along the locus of extrema of the response functions at the extrapolated $P_C(N \to \infty)$. From Fig.s 2, 3, and 4, we estimate $T_C(P_C^\infty)|_{\rm extrema} = 186.7 \pm 1.1$ K. By adding $T_C(P_C^\infty)|_{\rm extrema}$ and neglecting $T_C(N = 512)$, we find agreement with the expected scaling law in Eq.(5) with $T_C = (186 \pm 4)$ K (Fig. 8b). Here, the error is likely underestimated for the added point and is taken as the largest among the data used in our fit. Therefore, we confirm that the water LLCP has the 3D Ising critical exponents and conclude that its critical parameters in the thermodynamic limit are $P_C = (174 \pm 14)$ MPa, and $T_C = (186 \pm 4)$ K.

IV. DISCUSSION

Remarkably, our calculations are consistent with a recent overall analysis of available experimental data concluding that the LLCP, if present, should be located between 180 and 200 MPa and at a temperature close to 190 K[81]. These critical parameters are compatible with our estimates, especially considering the approximations adopted in Ref.[81] and our extrapolation of T_C.

In particular, by recompiling data for the NMR proton chemical shift, the authors of Ref.[81] indicate a structural transition along a locus in the 205 K - 220 K temperature range below 200 MPa that disappears at higher P. This locus of maxima is a proxy for the Widom line because the variation of NMR proton chemical shift with T along isobars is proportional to the isobaric T-derivative of $N_{\rm HB}$[107] and, as discussed above, the latter is contributing to the extrema of the response functions. Therefore, our results, showing response functions extrema between 205 K and 220 K, are quantitatively consistent, within the statistical errors, with the experimental data in Ref.[81] over the entire range of positive pressures we explored.

Mishima has provided another LLCP estimate[95], suggesting that it should be located below approximately 130 MPa and above approximately 210 K (Fig. 9). This estimate is extrapolated from experimental data at high P and $T >$ 300 K[103], assuming that the liquid-liquid transition line is near the homogeneous nucleation line of the crystal. Although Mishima's estimate lies at higher T and lower P than the one reported in Ref.[81], it is encouraging that both estimates converge on the general observation that the critical point must be on the low-pressure, low-temperature side of the TMD line and close to the temperature of the homogeneous crystal nucleation T_h. This region in Fig. 9 is delimited, in pressure, by the "No TMD" constant-P line that marks the $P_{\rm TMD}^{\rm Max} \simeq 180$ MPa above which no TMD is extrapolated from experimental data and, in temperature, by the TMD line. Many models, with a few exceptions, satisfy this condition. Several estimates of the LLCP, including ours, lie at the high-P limit of the region very close to the slope change in the experimental T_h. Other predictions, instead, are between the two experimentally extrapolated estimates (Fig. 9).

It is also intriguing to note that experiments conducted on micro-sized water droplets[16] reveal structural changes in liquid water at temperature (205 ± 10) K. These structural changes are interpreted as consistent with crossing an LLPT at a pressure between 1 atm and 350 MPa. The calculations presented here show that, at that temperature and up to approximately 50 MPa, water exhibits the most significant structural change marked by the locus of $C_P^{\rm Max}$, which is a proxy to the Widom line[105]. Furthermore, along this line, we find that finite systems undergo macroscopic fluctuations extending over more than 10 nm, the approximate size of our largest sample.

When compared with other numerical models, our LLCP prediction is in good agreement with the approximate estimates from a few others, e.g., the classical polarizable

iAMOEBA[42] (Fig. 9). The iAMOEBA is parameterized using experimental data and high-level *ab initio* calculations, where cooperative effects are included[41]. The analysis of K_T and C_P from atomistic simulations of the iAMOEBA suggests that it exhibits an apparent divergent point around (175 ± 10) MPa, and (184 ± 3) K[42].

More recently, free energy calculations for 192 molecules of a machine-learned monatomic water model with three-body interactions (ML-BOP) for both liquid water and ice[48] have shown the occurrence of the LLCP at $P_C = (170 \pm 10)$ MPa and $T_C = (181 \pm 3)$ K[14]. This estimate is very close to our result.

Notably, both the iAMOEBA and the ML-BOP models include optimized many-body interactions (HB cooperativity). This is also true for our CVF model whose parameters were selected[66] based on *ab initio* energy decomposition analysis of small water clusters[108]. Therefore, the agreement of our LLCP estimate with those from other cooperative models might be because they have a similar intensity of HB cooperativity, consistent with previous research indicating the importance of many-body interactions in determining the LLCP[11].

On the other hand, our prediction of the LLCP is within the statistical error of the rigid TIP4P/Ice model, whose o. p. fluctuations analysis leads to an estimate of $P_C = (173.9 \pm 0.6)$ MPa and $T_C = (188 \pm 1)$ K[33]. The TIP4P/Ice model considered in Ref.[33] is parametrized to reproduce the crystal phase diagram of water[109]. However, Espinosa et al. have shown that the model must be shifted by 40 MPa to fit the liquid water equation of state and compressibility, leading to a different estimate of the LLCP around 125 MPa and 195 K[36]. This new prediction falls along the locus of $C_P^{\rm Max}(P)$ as our finite-size LLCP estimate for N =4,096 CVF water molecules. The absence of finite-size scaling analysis in Ref.[36] prevents a consistent comparison with the original TIP4P/Ice model[33] and the present work.

Similar considerations also hold for the TIP4P model, for which the LLCP has been estimated around 190 K and 150 MPa[37], a state point which falls along our $C_P^{\rm Max}(P)$ line. However, when the model is shifted[37] by +31 K and −73 MPa to match the TMD experimental data, the LLCP estimate moves far from our calculations.

Finally, we observe that the average value of our prediction for the critical pressure $P_C = (174 \pm 14)$ MPa falls below the limiting pressure for the density anomaly, $P_{\rm TMD}^{\rm Max} \simeq 180$ MPa, calculated in the framework of our model (Fig. S1). Experiments show a consistent behavior, with the TMD no longer evident above 180 MPa[81,82]. Additionally, there is a drastic change in the slope of the melting line from negative to positive in the (T,P) plane, below and above 200 MPa, respectively, as well as for the temperature of the homogeneous crystallization[81].

The negative slope is due to the density anomaly. It is a result of the anticorrelation between volume variation ΔV and entropy change ΔS at the melting line for the Clausius-Clapeyron equation, which is given by $dP/dT|_{\rm phase\ transition} = \Delta S/\Delta V$. A positive slope of the melting line is typical of normal liquids without density anomaly.

We expect a negative slope also for the LLPT as there is a similar $\Delta S/\Delta V$ between the high-T HDL and the low-T LDL phase. Therefore, in the thermodynamic limit, the LLPT should occur below the pressure where the melting line of water changes its slope and there is no TMD, between 200 MPa and $P_C = (174 \pm 14)$ MPa (Fig. 9).

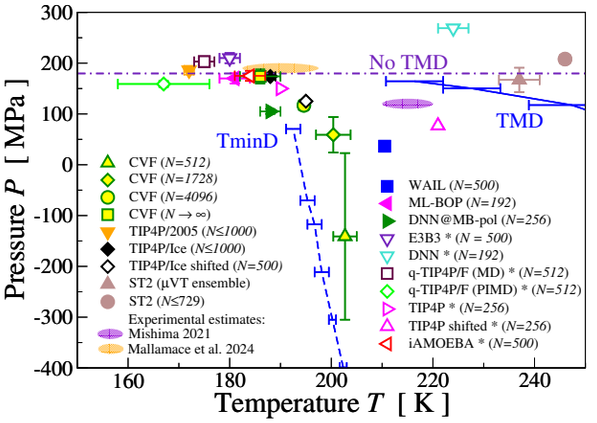

FIG. 9. **The CVF estimate of the LLCP in the thermodynamic limit compared to other models' predictions.** Our estimates of the critical parameters for different sizes N (yellow symbols, from bottom $N = 512$ to top 4,096) extrapolate in the thermodynamic limit to $T_C = (186 \pm 4)$ K and $P_C = (174 \pm 14)$ MPa (yellow square) close to the pressure $P_{\rm TMD}^{\rm Max} \simeq 180$ MPa above which liquid water, both in the experiments[81,82] and in our calculations (Fig. S1), displays no TMD (purple dot-dashed line). Our finite-size estimates fall along the locus of $C_P^{\rm Max}(P)$ from Fig. 2. Other estimates of the LLCP are for the TIP4P/2005 and TIP4P/Ice[33], TIP4P/Ice shifted[36], ST2 (μVT)[28], ST2 ($N \leq 729$)[32], WAIL[40], ML-BOP[14], DNN@MB-pol[49], E3B3[45], iAMOEBA[42], DNN[52], q-TIP4P/F (MD and PIMD)[53], TIP4P and TIP4P shifted[37], with sizes and symbols indicated in the legend. Asterisks (*) in the legend indicate approximate calculations. The orange-shaded area corresponds to the approximate estimate of the LLCP based on a recent analysis of a collection of experimental data in Ref.[81], while the purple-shaded area corresponds to the estimate based on extrapolated experimental data in Ref.[95].

It's fascinating to see that the TMD and TminD extrapolations are consistently converging toward our estimate of the LLCP (Fig. 9). This convergence suggests that the density anomaly region, which is delimited by the TMD and TminD lines, might originate from the LLCP, along with the Widom line. If this prediction is confirmed, it would provide compelling evidence of the relationship between the LLCP and the anomalies of water.

V. SUMMARY AND CONCLUSIONS

Experimental studies of the metastable region of liquid water are challenging[16,87,91] but fundamental for discriminating between different thermodynamic explanations of the water properties. Therefore, it is crucial to investigate the extrapolation of the equation of state of reliable models to the experimentally unexplored regions to address open questions related to the possible different thermodynamic scenarios[8,11,33].

In this work, we consider the CVF liquid water. This model provides a precise quantitative reproduction of the experimental data for the density, specific heat C_P, thermal expansion coefficient α_P, and compressibility K_T of liquid water with an unprecedented level of accuracy around ambient conditions over a temperature range of roughly 60 degrees at atmospheric pressure and up to 50 MPa[66]. As a result, it is one of the most reliable molecular models for liquid water at equilibrium. Here, we examine its phase diagram upon supercooling and stretching.

We analyze how the response functions, C_P, α_P, and K_T, change at supercooled temperatures by varying the pressure from negative to positive. We find the loci of response functions extrema and verify their consistency with general thermodynamic relations and the available experimental data.

Our results show that all the loci of extrema converge, within the statistical errors, to one single line that extends from positive pressure to moderately negative for the finite-size systems we consider here. Along the common locus of the extrema, we find that the liquid flips in energy and density between HDL-like and LDL-like states, as expected along the LLPT line. Furthermore, the Gibbs free energy calculated at the end of this line displays two minima as near an LLCP between the LDL and HDL.

Through a detailed scaling analysis, we find that the finite-size effects are significant. Still, the water LLCP also exists in the thermodynamic limit and belongs to the 3D Ising universality class. The critical parameters extrapolate to $T_C = (186 \pm 4)$ K and $P_C = (174 \pm 14)$ MPa.

Several recent studies of water models with different degrees of coarse-graining support the prediction of an LLCP. Our estimate of (T_C, P_C) is consistent with those for two cooperative models that optimize the many-body interactions, the iAMOEBA[42] and the ML-BOP[14]. General arguments[11] suggest that they have an intensity of HB cooperativity comparable to that of the CVF model. Intriguingly, these three models are based on a combination of experimental data and *ab initio* or machine-learning optimizations. They stand out for their quantitative agreement for the water density, although the CVF outperforms the others for the response functions. Therefore, the CVF model is reliable around ambient conditions and also comparable to optimized models in the metastable region.

The consistency among these models that optimize the many-body interactions and agree quantitatively with the water equation of state highlights the importance of hydrogen-bond cooperativity in explaining water anomalies. Previous theoretical studies have shown that scenarios without the LLCP are thermodynamically consistent and can also explain the water anomalies. However, these scenarios are excluded when cooperativity is considered and has a moderate intensity as in the present model[11].

Our LLCP estimate is also consistent with that of the TIP4P/Ice optimized for the solid phases[33], but not with the TIP4P/Ice shifted, optimized for liquid water[36]. However, the latter has critical parameters similar to our calculations for finite systems.

Furthermore, experiments[16] on supercooled water droplets show significant structural changes at pressures and temperatures corresponding to our estimate for the C_P maxima. Therefore, our work suggests an explanation for the results in Ref.[16] that, although alternative, is still consistent with the LLCP's existence.

Extrapolated experimental data allow Mishima to conclude that the LLCP should be on the low$T$, low-P side of the TMD line[95], consistent with our calculations. However, what is even more compelling is that our prediction for the LLCP matches, within the statistical error, with the estimate based on a comprehensive set of measurements recently analyzed[81]. The study also reviews data demonstrating significant ordering of the HB network over a range of pressures and temperatures[81], consistent with our estimates for the HB structuring, the extrema of the response functions, and the Widom line.

Finally, our prediction for the LLCP approaches the pressure limit where no TMD is found in the model[66] and the experiments[81,82] and the melting line changes its slope. Based on this, the LLPT should occur between 200 MPa and $P_C = (174 \pm 14)$ MPa, and it should lie with the LLCP at the convergence of the TMD and the TminD lines, providing persuasive evidence on the origin of the anomalies of water.

On a more applicative side, this study shows that a water model with a) high quantitative accuracy and transferability in a broad thermodynamic range around ambient conditions, b) capability of large-scale free-energy calculations, and c) computationally efficiency is also able to explore the metastable phases of water providing reliable calculations.

Our findings indicate that the hydrogen bond network can develop significant cooperative fluctuations at scales larger than 10nm when exposed to supercooled temperatures of around 205 K and pressure up to 50 MPa. These thermodynamic values are widely used in biostorage technology for cryopreservation of genetic material, biological tissues, and medications. Hence, it is crucial to understand the density fluctuations under these conditions to ensure long-term biopreservation without causing any cryo-injury[110].

Furthermore, an advantage of the CVF model is its ability to calculate free energy for systems containing millions of molecules efficiently. This feature is particularly useful for investigating large hydrated systems in various fields without requiring expensive computational resources or long real-time simulations. Such studies can address important questions relevant to nanotechnology[111–113] and biophysics[114,115], which often face limitations with conventional computational approaches[116–119]. While the CVF model is currently optimized only for bulk water, it has demonstrated great potential in these fields, providing many qualitative and semi-quantitative results[120–126]. Further studies are required to achieve quantitative predictions with hydrated interfaces.

SUPPLEMENTARY INFORMATION

See Supplementary Information for Tables S1 and S2 and Figures S1 – S4.

ACKNOWLEDGMENTS

We acknowledge Mariavittoria Franzese for the artistic interpretation of the highlight image of this work. L.E.C. acknowledges support from the Universitat de Barcelona grant no. 5757200 APIF_18_19. G.F. acknowledges the support by MCIN/AEI/ 10.13039/ 501100011033 and "ERDF A way of making Europe" grant number PID2021-124297NB-C31, by the Ministry of Universities 2023-2024 Mobility Subprogram within the Talent and its Employability Promotion State Program (PEICTI 2021-2023), and by the Visitor Program of the Max Planck Institute for The Physics of Complex Systems for supporting a visit started in November 2022.

AUTHOR DECLARATION

Conflict of interest

The authors have no conflict of interest to disclose.

Author contributions

L.E.C.: Investigation, Software, Methodology, Analysis, Writing – review & editing. G.F.: Conceptualization, Investigation, Methodology, Analysis, Writing – review & editing, Supervision, Funding acquisition.

DATA AVAILABILITY STATEMENT

The data supporting this study's findings are openly available at https://figshare.com/s/e5aafde37e8c7ffcf2be. The code and analysis script to reproduce the findings of this study are openly available at https://github.com/lcoronas/CVFBulkWater/.

Appendix A: The CVF model

A detailed description of the model with a full justification for its parameters is given in Ref.[66]. Here, we briefly define the model, its variables, and its parameters.

The model assumes that at constant temperature T and pressure P, N water molecules are distributed in a variable volume $V(T,P)$. The entire V is partitioned into cells $i \in [1,...,\mathscr{N}]$, with $\mathscr{N} \geq N$, each containing at most one molecule. Here, we set $\mathscr{N} = N$. Each cell has volume $v \equiv V/\mathscr{N} \geq v_0$, where $v_0 \equiv r_0^d$ is the van der Waals volume of one molecule, with $r_0 \equiv 2.9$ Å and d is the Euclidean dimension.

The CVF model coarse-grains the positions of the molecules, with $r \equiv v^{1/d}$ corresponding to the average distance between two neighboring molecules. The van der Waals interaction, modeled with the Lennard-Jones potential with an energy parameter $\varepsilon \equiv 5.5$ kJ/mol[66], determines the value of $v(T,P)$ and the homogeneous component of the density v_0/v, that is discretized with an index $n_i = 0$ if $v_0/v \leq 0.5$ (gas-like density), and $n_i = 1$ (liquid-like density) otherwise, for each cell and molecule i. The heterogeneous component of the density is associated with the number of HBs each molecule forms, as we discuss in the following.

The model separates the HB interaction into two Hamiltonian terms: the directional (covalent) component and the cooperativity component, which is much weaker than the first and is due to many-body correlations. They are described in terms of a set of *bonding* σ_{ij} variables. Each water molecule i has a bonding variable $\sigma_{ij} \in [1,...,q]$ for each water molecule j that is its neighbor. Consistent with the experiments, the model assumes that each water molecule can form only four tetrahedral HBs.

A HB is formed only if two neighboring molecules have the facing bonding variables in the same state, i.e., $\sigma_{ij} = \sigma_{ji}$. Debye-Waller factors estimate[127] and calculations[128] show that only $1/6$ of the entire range of possible values $[0,360^\circ]$ of the $\widehat{\mathrm{OOH}}$ angle between two molecules is associated with a bonded state. Therefore, the model sets $q = 6$ to account for this constraint.

Furthermore, consistent with calculations[129–131], the HB has a negligible energy, i.e., is broken, for O–O larger than a distance $r_{\max}$. The CVF model sets $r_{\max} \simeq 3.65$Å. This choice guarantees that, in the homogeneous system, the HB breaks if the O–O distance between two bonded molecules becomes $r > r_{\max}$, i.e., $v_0/v \equiv r_0^3/r^3 < 0.5$, then $n_i = 0\ \forall i$. If, instead, $r \leq r_{\max}$ then $n_i = 1\ \forall i$, and $n_i n_j = 1$, allowing the HB formation. Hence, n_i is a *bonding* index.

In a cubic lattice, each molecule has six nearest neighbors. However, a water molecule cannot form more than four HBs. For this reason, we introduce a set of *allowing* variables $\eta_{ij} \in \{0,1\}$, where 0 denotes a forbidden bond between molecules i and j, and 1 denotes an allowed bond. By construction, for each molecule i, four of the six variables η_{ij} are set to 1, while the other two are 0, with $\eta_{ij} = \eta_{ji}\ \forall ij$. Ref.[69] describes an algorithm for generating valid configurations of the η_{ij} variables.

The total number of HBs is, therefore,

$$N_{\mathrm{HB}} = \sum_{<i,j>} n_i n_j \eta_{ij} \delta_{\sigma_{ij},\sigma_{ji}} \tag{A1}$$

where the sum is over the nearest neighbor molecules and $\delta_{a,b} = 1$ if $a = b$, and 0 otherwise. The Hamiltonian term corresponding to the directional component of the HB interaction is pair-additive and linear in N_{HB},

$$\mathscr{H}_{\mathrm{HB}} \equiv -J N_{\mathrm{HB}}, \tag{A2}$$

where J is set to 11 kJ/mol[66].

The cooperative component of the HB interaction is given by a five-body term, consistent with the analysis of polarizable water clusters[132],

$$\mathscr{H}_\sigma \equiv -J_\sigma N_\sigma \equiv -J_\sigma \sum_i n_i \sum_{(k,l)_i} \delta_{\sigma_{ik},\sigma_{il}}, \tag{A3}$$

where $(k,l)_i$ indicates all possible pairs of bonding variables of the i-th water molecules, and $J_\sigma = 1.76$ kJ/mol is set[66]

based on ALMOEDA analysis[108] of density functional theory calculations on water clusters[133].

Finally, the total volume of the system is

$$V_{\rm Tot} \equiv V + v_{\rm HB} N_{\rm HB}, \tag{A4}$$

where $v_{\rm HB} = 14.4$ Å^3 accounts for the local decrease in density due to HB formation[134]. Hence, $V_{\rm Tot}$ includes the local heterogeneity in the density field due to the HBs.

Appendix B: The order parameter

We consider $Q(\bar{e},\bar{\rho})$, where $\bar{e}$ and $\bar{\rho}$ are dimensionless quantity, and rotate it using the 2D Euclidean rotation matrix, $\mathscr{M} = \bar{e}\sin(\alpha) + \bar{\rho}\cos(\alpha)$. Therefore, we define $M(s) \equiv \mathscr{M}/\cos(\alpha) = \bar{\rho} + s\bar{e}$, where $s \equiv \tan(\alpha)$.

Our joint probability distribution $Q(e,\rho)$ has a strongly asymmetric shape, as evident from the asymmetry between the two basins of attractions of ΔG (Fig.6), considering that $Q(e,\rho) = \exp[-\Delta G(e,\rho)/k_B T]$. Specifically, the basin for the LDL state is broader than that for the HDL.

Therefore, to make the two basins more symmetric, we need to consider only rotations for $\alpha \in [\pi/2, \pi]$ and $[3\pi/2, 2\pi]$, hence $s < 0$. We check that the sign of s depends on the model's parameter choice.

For each size N, we test a candidate $(T_C(N), P_C(N))$ by rescaling M as $m \equiv B(M - M_C)$, where B and M_C (in Table S2 of the Supplementary Information) make $Q(m)$ with zero mean and unit variance. However, we realize that any combination of $(T_C(N), P_C(N))$ and $s(N)$ allows us to fit $Q(m)$ to Q_3 only partially. Specifically, we find that the tails of $Q(m)$ are overrated, and the peaks are underrated (Fig. 10a red squares).

We, therefore, test alternative functional forms $X(m)$ for the rescaled o. p. in such a way to best fit $Q(X)$ to Q_3. First, we observe that $Q(m) - Q_3 = 0$ for $m = 0$ and $m = \pm m_0$ (Fig. 10a). Thus, we consider only transformations with fixed points in $m = 0$ and $\pm m_0$. Furthermore, $X(m)$ must slightly shrink the tails ($|m| > m_0$) and stretch the peaks ($|m| < m_0$) of our $Q(m)$ to fit Q_3 (Fig. 10a).

Under these considerations, we find that the function

$$X(m) \equiv \alpha_0 \lambda^2 \sin\left(\frac{m}{\lambda}\right) + \alpha_1 m \tag{B1}$$

fits well to our purposes because, when $\alpha_1 = 1$ and $\lambda = m_0/\pi$, it has fixed points $\forall m = k \cdot m_0$, with $k \in \mathbb{Z}$. Moreover, the sinus alternatively changes its sign shifting m as convenient, while α_0 controls the amplitude of the modulation (Fig. 10b).

Next, by observing that $(\alpha_0, \alpha_1) = (1,1)$ is the best combination and that the modulation requires a further normalization to fit Q_3, we get the final expression for the rescaled o. p. as

$$x \equiv B_0(X(m) - X_C) \tag{B2}$$

where the constant B_0 and X_C are given in the Table S2 of the Supplementary Information, together with λ, for all the values of N.

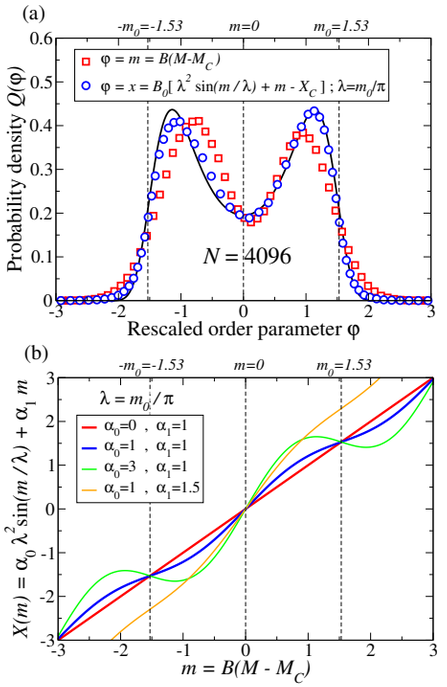

FIG. 10. **Rescaling of the order parameter M and comparison with Q_3.** (a) Comparison between the probability distribution $Q(m)$ (red squares) for the rescaled $m \equiv B(M - M_C)$; $Q(x)$ (blue circles) for the rescaled o. p. x defined in Eq.(B2); and $Q_3(\varphi)$ (black line). Symbols are calculated for the CVF model with N =4,096 near the estimated $(T_C(N), P_C(N))$. $Q(m)$ coincides with Q_3 at $m = 0$ and $m_0 = \pm 1.53$. (b) The function $X(m)$ in Eq.(B1) modulates m allowing us to best fit Q to Q_3. All the curves are for $\lambda = m_0/\pi$ (con $m_0 = 1.53/\pi$ for N =4,096) so that, when $\alpha_1 = 1$, $X(m) = m$ at $m = 0$ and $\pm m_0$ (marked by the dashed vertical lines). For $(\alpha_0, \alpha_1) = (0,1)$, it is $X(m) = m$ (red line). For other combinations with $\alpha_1 = 1$, α_0 controls the amplitude of the m modulation. The combination $(\alpha_0, \alpha_1) = (1,1)$ is our best choice (blue line), and it is used to calculate the distribution Q with blue squares in panel (a). Other combinations (α_0, α_1) are shown for comparison (green and orange lines).

[1] K. Amann-Winkel, R. Böhmer, F. Fujara, C. Gainaru, B. Geil, and T. Loerting, Rev. Mod. Phys. **88**, 011002 (2016).
[2] P. H. Handle, T. Loerting, and F. Sciortino, P. Natl. Acad. Sci. USA **114**, 13336 (2017).
[3] J. C. Palmer, P. H. Poole, F. Sciortino, and P. G. Debenedetti, *Chem. Rev.*, Chem. Rev. **118**, 9129 (2018).
[4] P. Gallo, J. Bachler, L. E. Bove, R. Böhmer, G. Camisasca, L. E. Coronas, H. R. Corti, I. de Almeida Ribeiro, M. de Koning, G. Franzese, V. Fuentes-Landete, C. Gainaru, T. Loerting, J. M. M. de Oca, P. H. Poole, M. Rovere, F. Sciortino, C. M. Tonauer, and G. A. Appignanesi, Euro. Phys. J. E **44**, 143 (2021).
[5] M. Chaplin, Nat. Rev. Mol. Cell. Biol. **7**, 861 (2006).
[6] P. G. Debenedetti, *Metastable Liquids. Concepts and Principles* (Princeton University Press, Princeton, NJ, 1996).
[7] R. J. Speedy, J. Phys. Chem. **86**, 3002 (1982).
[8] P. Poole, F. Sciortino, U. Essmann, and H. Stanley, Nature **360**, 324 (1992).
[9] S. Sastry, P. G. Debenedetti, F. Sciortino, and H. E. Stanley, Phys. Rev. E **53**, 6144 (1996).
[10] C. A. Angell, Science **319**, 582 (2008).
[11] K. Stokely, M. G. Mazza, H. E. Stanley, and F. G., P. Natl. Acad. Sci. USA **107**, 1301 (2010).

[12]P. Barnes, J. L. Finney, J. D. Nicholas, and J. E. Quinn, Nature **282**, 459 (1979).
[13]Y. Shi, H. Scheiber, and R. Z. Khaliullin, J. Phys. Chem. A **122**, 7482 (2018).
[14]D. Dhabal, R. Kumar, and V. Molinero, ChemRxiv (2024), 10.26434/chemrxiv-2023-x8vxb-v2.
[15]J. C. Palmer, F. Martelli, Y. Liu, R. Car, A. Z. Panagiotopoulos, and P. G. Debenedetti, Nature **510**, 385 (2014).
[16]K. H. Kim, K. Amann-Winkel, N. Giovambattista, A. Späh, F. Perakis, H. Pathak, M. L. Parada, C. Yang, D. Mariedahl, T. Eklund, T. J. Lane, S. You, S. Jeong, M. Weston, J. H. Lee, I. Eom, M. Kim, J. Park, S. H. Chun, P. H. Poole, and A. Nilsson, Science **370**, 978 (2020).
[17]W. Dong, Z. Wu, J. Ge, S. Liu, S. Lan, E. P. Gilbert, Y. Ren, D. Ma, and X.-L. Wang, Appl. Phys. Lett. **118**, 191901 (2021).
[18]M. A. Harris, T. Kinsey, D. V. Wagle, G. A. Baker, and J. Sangoro, P. Natl. Acad. Sci. USA **118**, e2020878118 (2021).
[19]P. D. Lane, J. Reichenbach, A. J. Farrell, L. A. I. Ramakers, K. Adamczyk, N. T. Hunt, and K. Wynne, Phys. Chem. Chem. Phys. **22**, 9438 (2020).
[20]Y. Suzuki, P. Natl. Acad. Sci. USA **119** (2022), 10.1073/pnas.2113411119.
[21]J. Bachler, L.-R. Fidler, and T. Loerting, Phys. Rev. E **102**, 060601 (2020).
[22]K. Winkel, E. Mayer, and T. Loerting, J. Phys. Chem. B **115**, 14141 (2011), pMID: 21793514.
[23]F. Perakis, K. Amann-Winkel, F. Lehmkühler, M. Sprung, D. Mariedahl, J. A. Sellberg, H. Pathak, A. Späh, F. Cavalca, D. Schlesinger, A. Ricci, A. Jain, B. Massani, F. Aubree, C. J. Benmore, T. Loerting, G. Grübel, L. G. M. Pettersson, and A. Nilsson, P. Natl. Acad. Sci. USA **114**, 8193 (2017).
[24]K. H. Kim, A. Späh, H. Pathak, F. Perakis, D. Mariedahl, K. Amann-Winkel, J. A. Sellberg, J. H. Lee, S. Kim, J. Park, K. H. Nam, T. Katayama, and A. Nilsson, Science **358**, 1589 (2017).
[25]F. Caupin, V. Holten, C. Qiu, E. Guillerm, M. Wilke, M. Frenz, J. Teixeira, and A. K. Soper, Science **360** (2018).
[26]K. H. Kim, A. Späh, H. Pathak, F. Perakis, D. Mariedahl, K. Amann-Winkel, J. A. Sellberg, J. H. Lee, S. Kim, J. Park, K. H. Nam, T. Katayama, and A. Nilsson, Science **360** (2018).
[27]A. Nilsson, J. Non-Cryst. Solids: X **14**, 100095 (2022).
[28]Y. Liu, A. Z. Panagiotopoulos, and P. G. Debenedetti, J. Chem. Phys. **131**, 104508 (2009).
[29]F. Sciortino, I. Saika-Voivod, and P. H. Poole, Phys. Chem. Chem. Phys. **13**, 19759 (2011).
[30]Y. Liu, J. C. Palmer, A. Z. Panagiotopoulos, and P. G. Debenedetti, J. Chem. Phys. **137**, 214505 (2012).
[31]T. A. Kesselring, G. Franzese, S. V. Buldyrev, H. J. Herrmann, and H. E. Stanley, Sci. Rep. **2**, 474 (2012).
[32]T. A. Kesselring, E. Lascaris, G. Franzese, S. V. Buldyrev, H. J. Herrmann, and H. E. Stanley, J. Chem. Phys. **138**, 244506 (2013).
[33]P. G. Debenedetti, F. Sciortino, and G. H. Zerze, Science **369**, 289 (2020).
[34]F. Sciortino, I. Gartner, Thomas E., and P. G. Debenedetti, J. Chem. Phys. **160**, 104501 (2024).
[35]R. Foffi, J. Russo, and F. Sciortino, J. Chem. Phys. **154**, 184506 (2021).
[36]J. R. Espinosa, J. L. F. Abascal, L. F. Sedano, E. Sanz, and C. Vega, J. Chem. Phys. **158**, 204505 (2023).
[37]D. Corradini, M. Rovere, and P. Gallo, J. Chem. Phys. **132**, 134508 (2010).
[38]S. V. Buldyrev and G. Franzese, *7th IDMRCS: Relaxation in Complex Systems*, J. Non-Cryst. Solids **407**, 392 (2015).
[39]A. Neophytou, D. Chakrabarti, and F. Sciortino, Nat. Phys. **18**, 1248 (2022).
[40]J. Weis, F. Sciortino, A. Z. Panagiotopoulos, and P. G. Debenedetti, J. Chem. Phys. **157**, 024502 (2022).
[41]L.-P. Wang, T. Head-Gordon, J. W. Ponder, P. Ren, J. D. Chodera, P. K. Eastman, T. J. Martinez, and V. S. Pande, J. Phys. Chem. B **117**, 9956 (2013).
[42]H. Pathak, J. C. Palmer, D. Schlesinger, K. T. Wikfeldt, J. A. Sellberg, L. G. M. Pettersson, and A. Nilsson, J. Chem. Phys. **145**, 134507 (2016).
[43]V. Bianco and G. Franzese, Sci. Rep. **4**, 4440 EP (2014).
[44]N. J. Hestand and J. L. Skinner, J. Chem. Phys. **149**, 140901 (2018).
[45]Y. Ni and J. L. Skinner, J. Chem. Phys. **144**, 214501 (2016).
[46]J. L. F. Abascal and C. Vega, J. Chem. Phys. **123**, 234505 (2005).
[47]A. Neophytou and F. Sciortino, J. Chem. Phys. **160**, 114502 (2024).
[48]H. Chan, M. J. Cherukara, B. Narayanan, T. D. Loeffler, C. Benmore, S. K. Gray, and S. K. R. S. Sankaranarayanan, Nat. Commun. **10**, 379 (2019).
[49]F. Sciortino, Y. Zhai, S. L. Bore, and F. Paesani, ChemRxiv (2024), 10.26434/chemrxiv-2024-dqqws.
[50]S. L. Bore and F. Paesani, Nat. Commun. **14**, 3349 (2023).
[51]J. W. Biddle, R. S. Singh, E. M. Sparano, F. Ricci, M. A. González, C. Valeriani, J. L. F. Abascal, P. G. Debenedetti, M. A. Anisimov, and F. Caupin, J. Chem. Phys. **146**, 034502 (2017).
[52]T. E. Gartner, L. Zhang, P. M. Piaggi, R. Car, A. Z. Panagiotopoulos, and P. G. Debenedetti, P. Natl. Acad. Sci. USA **117**, 26040 (2020).
[53]A. Eltareb, G. E. Lopez, and N. Giovambattista, Sci. Rep. **12**, 6004 (2022).
[54]R. S. Singh, J. W. Biddle, P. G. Debenedetti, and M. A. Anisimov, J. Chem. Phys. **144**, 144504 (2016).
[55]H. E. Stanley and J. Teixeira, *J. Chem. Phys.*, J. Chem. Phys. **73**, 3404 (1980).
[56]R. Lamanna, M. Delmelle, and S. Cannistraro, Phys. Rev. E **49**, 2841 (1994).
[57]S. Strässler and C. Kittel, Phys. Rev. **139**, A758 (1965).
[58]E. Rapoport, J. Chem. Phys. **46**, 2891 (1967).
[59]H. Tanaka, Phys. Rev. E **62**, 6968 (2000).
[60]G. Franzese, M. Yamada, and H. E. Stanley, AIP Conf. Proc. **519**, 281 (2000).
[61]G. Franzese and H. Eugene Stanley, Physica A: Stat. Mech. Appl. **314**, 508 (2002).
[62]H. Tanaka, *J. Chem. Phys.*, J. Chem. Phys. **153**, 130901 (2020).
[63]P. Gallo, F. Sciortino, P. Tartaglia, and S. H. Chen, Phys. Rev. Lett. **76**, 2730 (1996).
[64]D. T. Limmer and D. Chandler, J. Chem. Phys. **135**, 134503 (2011).
[65]S. D. Overduin and G. N. Patey, J. Chem. Phys. **138**, 184502 (2013).
[66]L. E. Coronas, O. Vilanova, and G. Franzese, A transferable molecular model for accurate thermodynamic studies of water in large-scale systems (2024), https://doi.org/10.21203/rs.3.rs-4243098/v1.
[67]O. Vilanova and G. Franzese, arXiv:1102.2864 (2011).
[68]V. Bianco, O. Vilanova, and G. Franzese, "Polyamorphism and polymorphism of a confined water monolayer: liquid-liquid critical point, liquid-crystal and crystal-crystal phase transitions," in *Perspectives and Challenges in Statistical Physics and Complex Systems for the Next Decade* (WORLD SCIENTIFIC, 2014) pp. 126–149.
[69]L. E. Coronas, *Calculations of water free energy in bulk and large biological systems*, Ph.D. thesis, Facultat de Física, Universitat de Barcelona, Barcelona, Spain (2023).
[70]Y. Liu, A. Z. Panagiotopoulos, and P. G. Debenedetti, J. Chem. Phys. **132**, 144107 (2010).
[71]M. G. Mazza, K. Stokely, E. G. Strekalova, H. E. Stanley, and G. Franzese, *Special issue based on the Conference on Computational Physics 2008 - CCP 2008*, Comput. Phys. Commun. **180**, 497 (2009).
[72]D. P. Landau and K. Binder, "A guide to monte carlo simulations in statistical physics," (Cambridge University Press, 2021) Chap. 5, 3rd ed.
[73]V. Bianco and G. Franzese, J. Mol. Liq. **285**, 727 (2019).
[74]G. Franzese and F. de los Santos, J. Phys.: Cond. Matt. **21**, 504107 (2009).
[75]P. G. Debenedetti and H. E. Stanley, Phys. Today **56**, 40 (2003).
[76]U. Wolff, Phys. Rev. Lett. **62**, 361 (1989).
[77]N. Wilding and K. Binder, Physica A: Stat. Mech. Appl. **231**, 439 (1996).
[78]P. Gallo and F. Sciortino, Phys. Rev. Lett. **109**, 177801 (2012).
[79]Y. Goswami and S. Sastry, PNAS Nexus **1** (2022), 10.1093/pnasnexus/pgac204.
[80]A. Z. Panagiotopoulos, J. Phys.: Cond. Matt. **12**, R25 (2000).
[81]F. Mallamace and D. Mallamace, J. Chem. Phys. **160**, 184501 (2024).
[82]O. Mishima, J. Chem. Phys. **133**, 144503 (2010).
[83]H. Tanaka, Nature **380**, 328 (1996).
[84]C. Lobban, J. L. Finney, and W. F. Kuhs, Nature **391**, 268 (1998).
[85]T. M. Gasser, A. V. Thoeny, A. D. Fortes, and T. Loerting, Nat. Commun. **12**, 1128 (2021).
[86]G. Pallares, M. El Mekki Azouzi, M. A. González, J. L. Aragones, J. F. Abascal, C. Valeriani, and F. Caupin, P. Natl. Acad. Sci. USA **111**, 7936 (2014).
[87]V. Holten, C. Qiu, E. Guillerm, M. Wilke, J. Rička, M. Frenz, and F. Caupin, *J. Phys. Chem. Lett.*, J. Phys. Chem. Lett. **8**, 5519 (2017).
[88]I. Stepanov, Results Phys. **4**, 28 (2014).
[89]C.-W. Lin and J. P. M. Trusler, J. Chem. Phys. **136**, 094511 (2012).
[90]E. W. Lemmon and A. H. Harvey, in *CRC Handbook of Chemistry and*

Physics, edited by J. R. Rumble (CRC Press/Taylor & Francis, Boca Raton, FL, 2020) 101st ed., pp. 918–921.
[91]H. Pathak, A. Späh, N. Esmaeildoost, J. A. Sellberg, K. H. Kim, F. Perakis, K. Amann-Winkel, M. Ladd-Parada, J. Koliyadu, T. J. Lane, C. Yang, H. T. Lemke, A. R. Oggenfuss, P. J. M. Johnson, Y. Deng, S. Zerdane, R. Mankowsky, P. Beaud, and A. Nilsson, P. Natl. Acad. Sci. USA **118**, e2018379118 (2021).
[92]R. J. Speedy, *J. Phys. Chem.*, J. Phys. Chem. **86**, 982 (1982).
[93]P. H. Poole, I. Saika-Voivod, and F. Sciortino, J. Phys.: Cond. Matt. **17**, L431 (2005).
[94]J. R. Errington and P. G. Debenedetti, Nature **409**, 318 (2001).
[95]O. Mishima, "Volume of liquid water and amorphous ices," in *Liquid-Phase Transition in Water* (Springer Japan, Tokyo, 2021) pp. 29–58.
[96]L. P. N. Rebelo, P. G. Debenedetti, and S. Sastry, J. Chem. Phys. **109**, 626 (1998).
[97]M. G. Mazza, K. Stokely, H. E. Stanley, and G. Franzese, J. Chem. Phys. **137**, 204502 (2012).
[98]M. G. Mazza, K. Stokely, S. E. Pagnotta, F. Bruni, H. E. Stanley, and G. Franzese, P. Natl. Acad. Sci. USA **108**, 19873 (2011).
[99]A. Cupane, M. Fomina, and G. Schirò, J. Chem. Phys. **141**, 18C510 (2014).
[100]F. Mallamace, C. Corsaro, D. Mallamace, E. Fazio, S.-H. Chen, and A. Cupane, Int. J. Mol. Sci. **21**, 5908 (2020).
[101]M. A. González, C. Valeriani, F. Caupin, and J. L. F. Abascal, J. Chem. Phys. **145**, 054505 (2016).
[102]V. Holten, J. C. Palmer, P. H. Poole, P. G. Debenedetti, and M. A. Anisimov, J. Chem. Phys. **140**, 104502 (2014).
[103]L. Ter Minassian, P. Pruzan, and A. Soulard, J. Chem. Phys. **75**, 3064 (1981).
[104]R. A. Fine and F. J. Millero, J. Chem. Phys. **59**, 5529 (1973).
[105]G. Franzese and H. E. Stanley, J. Phys.: Cond. Matt. **19**, 205126 (2007).
[106]J. Luo, L. Xu, E. Lascaris, H. E. Stanley, and S. V. Buldyrev, Phys. Rev. Lett. **112**, 135701 (2014).
[107]F. Mallamace, C. Corsaro, M. Broccio, C. Branca, N. González-Segredo, J. Spooren, S. H. Chen, and H. E. Stanley, P. Natl. Acad. Sci. USA **105**, 12725 (2008).
[108]R. Z. Khaliullin and T. D. Kühne, Phys. Chem. Chem. Phys. **15**, 15746 (2013).
[109]J. L. F. Abascal, E. Sanz, R. García Fernández, and C. Vega, J. Chem. Phys. **122**, 234511 (2005).
[110]S. Guo and A. Zhang, Int. J. Refrig. **157**, 53 (2024).
[111]N. Kavokine, M.-L. Bocquet, and L. Bocquet, Nature **602**, 84 (2022).
[112]R. Bellido-Peralta, F. Leoni, C. Calero, and G. Franzese, J. Mol. Liq. **391**, 123356 (2023).
[113]F. Spinozzi, P. Moretti, D. R. Perinelli, G. Corucci, P. Piergiovanni, H. Amenitsch, G. A. Sancini, G. Franzese, and P. Blasi, J. Colloid Interf. Sci. **662**, 446 (2024).
[114]G. Franzese, K. Stokely, X. Q. Chu, P. Kumar, M. G. Mazza, S. H. Chen, and H. E. Stanley, J. Phys.: Cond. Matt. **20**, 494210 (2008).
[115]C. Camilloni and F. Pietrucci, Adv. Phys. X **3**, 1477531 (2018).
[116]R. B. Best, W. Zheng, and J. Mittal, *J. Chem. Theor. Comput.*, J. Chem. Theor. Comput. **10**, 5113 (2014).
[117]S. Piana, A. G. Donchev, P. Robustelli, and D. E. Shaw, J. Phys. Chem. B **119**, 5113 (2015).
[118]J. Huang, S. Rauscher, G. Nawrocki, T. Ran, M. Feig, B. L. de Groot, H. Grubmüller, and A. D. MacKerell, Nat. Methods **14**, 71 (2017).
[119]F. Aydin, R. Sun, and J. M. Swanson, Biophys. J. **117**, 87 (2019).
[120]V. Bianco and G. Franzese, Phys. Rev. Lett. **115**, 108101 (2015).
[121]V. Bianco, G. Franzese, C. Dellago, and I. Coluzza, Phys. Rev. X **7**, 021047 (2017).
[122]V. Bianco, N. Pagès-Gelabert, I. Coluzza, and G. Franzese, *Recent Progresses on the Experimental & Theoretical-Computational Techniques for the Study of Liquids and Supercritical Fluids. From Simple to Complex Systems*, J. Mol. Liq. **245**, 129 (2017).
[123]V. Bianco, M. Alonso-Navarro, D. Di Silvio, S. Moya, A. L. Cortajarena, and I. Coluzza, *J. Phys. Chem. Lett.*, J. Phys. Chem. Lett. **10**, 4800 (2019).
[124]V. Bianco, G. Franzese, and I. Coluzza, *ChemPhysChem*, ChemPhysChem **21**, 377 (2020).
[125]D. March, V. Bianco, and G. Franzese, Polymers **13**, 156 (2021).
[126]B. Durà-Faulí, V. Bianco, and G. Franzese, J. Phys. Chem. B **127**, 5541 (2023).
[127]J. Teixeira, M. C. Bellissent-Funel, and S. C. Chen, J. Phys.: Cond. Matt. **2** (1990).
[128]M. Ceriotti, J. Cuny, M. Parrinello, and D. E. Manolopoulos, P. Natl. Acad. Sci. USA **110**, 15591 (2013).
[129]A. Luzar and D. Chandler, Phys. Rev. Lett. **76**, 928 (1996).
[130]M. Hus and T. Urbic, J. Chem. Phys. **136**, 144305 (2012).
[131]C. Schran and D. Marx, Phys. Chem. Chem. Phys. **21**, 24967 (2019).
[132]D. Abella, G. Franzese, and J. Hernández-Rojas, ACS Nano **17**, 1959 (2023).
[133]E. A. Cobar, P. R. Horn, R. G. Bergman, and M. Head-Gordon, Phys. Chem. Chem. Phys. **14**, 15328 (2012).
[134]I. Skarmoutsos, G. Franzese, and E. Guardia, J. Mol. Liq. **364**, 119936 (2022).